

Cloud gap-filling with deep learning for improved grassland monitoring

Iason Tsardanidis^a, Alkiviadis Koukos^a, Vasileios Sitokonstantinou^b,
Thanassis Drivas^a, Charalampos Kontoes^a

^a*National Observatory of Athens, Operational Unit BEYOND Centre for Earth
Observation Research and Satellite Remote Sensing, Institute for Astronomy,
Astrophysics, Space Applications and Remote Sensing, 6 Karyistou
St., 11523, Athens, Greece*

^b*Image Processing Laboratory (IPL), Parc Científic, Universitat de València, 46980
Paterna, València, Spain*

Abstract

Uninterrupted optical image time series are crucial for the timely monitoring of agricultural land changes. However, the continuity of such time series is often disrupted by clouds. In response to this challenge, we propose a deep learning method that integrates cloud-free optical (Sentinel-2) observations and weather-independent (Sentinel-1) Synthetic Aperture Radar (SAR) data, using a combined Convolutional Neural Network (CNN)-Recurrent Neural Network (RNN) architecture to generate continuous Normalized Difference Vegetation Index (NDVI) time series. We emphasize the significance of observation continuity by assessing the impact of the generated time series on the detection of grassland mowing events. We focus on Lithuania, a country characterized by extensive cloud coverage, and compare our approach with alternative interpolation techniques (i.e., linear, Akima, quadratic). Our method surpasses these techniques, with an average MAE of 0.024 and R^2 of 0.92. It not only improves the accuracy of event detection tasks by em-

ploying a continuous time series, but also effectively filters out sudden shifts and noise originating from cloudy observations that cloud masks often fail to detect. A part of the code is accessible on [Github](#).

Keywords: Satellite image time series, Normalized difference vegetation index, Mowing detection, Synthetic aperture radar imagery, Image fusion

1. Introduction

Grasslands cover around one third of the global agricultural land and they play a key role in food production, animal biodiversity and global carbon cycle [1]. They provide a wide range of ecosystem services, such as (i) provision of fodder for livestock, (ii) wildlife habitats, (iii) filtering or retention functions of waterways and greenhouse gas emissions, (iv) carbon storage, (v) pest control, (vi) crop pollination and (vii) protection against soil erosion [2]. The 2013 reform of the Common Agricultural Policy (CAP) has emphasized on the importance of grassland use intensity by requiring a minimum number of mowing or grazing events. National paying agencies have been tasked with the monitoring of compliance with this minimum activity condition. This information is important for the consolidation of agro-ecological measures and conservation schemes with regards to climate change [3, 4].

The ever-increasing availability of remote sensing data has enabled the development of numerous competent agricultural monitoring systems. Most studies on grassland monitoring use remote sensing to address the problem of discriminating the different grassland categories (based on land cover, use intensity, etc.) and evaluate the various management strategies [5]. However, there are a few that focus on the quantification of grassland grazing intensity

and detection of mowing events. In most cases, optical Earth observation data (MODIS, RapidEye, Landsat 8, Sentinel-2, etc.) are exploited [6, 7]. A number of studies evaluate the mapping of the mowing or grazing frequency using statistical methods over multi-spectral image time series on regional or national scale [8, 9]. Therefore, relevant vegetation indices, such as the Normalized Difference Vegetation Index (NDVI), the Leaf Area Index (LAI) or others, are used to detect drastic changes in the grasslands vegetation cover, between consecutive observations, which is related to the amount of biomass removed.

Nevertheless, one of the main limitations of optical data is missing or invalid values caused by cloud coverage and unfavorable weather conditions. This problem is more evident in northern countries, where even the short revisit time of 5 days of Sentinel-2 can result in time series with long gaps [10]. Consequently, frequent cloud cover in these areas obstructs the detection of mowing practices, rendering algorithms reliant on optical data less effective in discerning these events [8]. Hence, there is a need to artificially reconstruct these missing or corrupted values. This reconstruction can be performed by using only optical data, only SAR data or a collaborative exploitation of both [11]. A dynamic combination of SAR with the available optical data can i) enrich the feature space and enhance the overall performance of downstream tasks and ii) fill in the missing values in optical products [12].

The most straightforward method for addressing gaps in optical data is through temporal gap-filling techniques that rely only on optical data, such as the linear (or splines) interpolation [13]. Despite the fact that these methods have been proved sufficient for several tasks [14, 15], in cases that we need to

precisely track crops phenology development or identify any abrupt changes (e.g., detection of an event, natural disasters etc.), crucial points may be left out, and as a result, the performance would be sub-optimal, especially when the gaps are long [16].

Similarly, the combination of various multi-sensor data can result in more dense satellite image time series (e.g., fusion of PlanetScope and Sentinel-2) which could, in turn, increase the number of cloud-free observations. However, there are still challenges that need to be taken into account, such as the different scales of spatial resolution [17] and the potential high financial cost of other sources [18] that acts as a barrier to the scalability of the methodologies. Additionally, complementary inputs from ancillary optical sensors usually require numerous pre-processing steps to achieve the same data distribution [19] and the provision of sufficient number of additional observations is at stake since they are affected by cloud coverage as well.

Contrary to the optical systems, SAR sensors can offer imagery at any time and under any weather circumstances, making them a very important source of information for agricultural monitoring in areas with frequent clouds [20]. Moreover, backscatter coefficients can detect the geometric, structural and dielectric properties of plants [21], rendering SAR data suitable for tasks such as crop classification [22] and grassland monitoring [23].

In this study, we utilise Sentinel-1 and Sentinel-2 time series data to optimize the filling of missing NDVI values. Our approach involves a deep learning architecture that combines Convolutional and Recurrent Neural Networks (CNN-RNN). Specifically, we integrate Sentinel-1 backscatter and coherence time series with the available Sentinel-2 NDVI images to construct continuous

NDVI time series of a fixed 6-day temporal resolution, focusing on grasslands across Lithuania. Then, we evaluate the impact of our generated continuous grassland time series in the downstream task of detecting grassland mowing. We choose the CNN-RNN architecture as it has been applied in the similar study of [24]. The main contributions of this study are summarized as follows:

1. Developed a CNN-RNN model that integrates Sentinel-1 and the cloud-free Sentinel-2 NDVI observations in order to construct continuous NDVI time series of a 6-day temporal step at the pixel level.
2. Assessed the performance of our cloud gap-filling method for different cloud coverage scenarios. Additionally, we performed a comparison analysis with other widely-used baseline interpolation methods.
3. Evaluated the added-value of utilizing the continuous NDVI time series on detecting grassland mowing events.

2. Related work

The reconstruction of optical images has been widely studied, with most papers focusing on spectral, temporal, or spectral-temporal methods. Among these, spectral-temporal methods offer the best performance [25]. Recently, there has been an increase in studies that specifically target NDVI reconstruction. The methods used by these studies can be split into three main groups; i) temporal-based, ii) frequency-based, and iii) hybrid [26]. When it comes to vegetation monitoring, the most common are the temporal-based methods. These methods exploit the phenological continuity of NDVI time series, but they lack precision when long temporal gaps are present. Frequency-based

methods have low computational complexity and are easy to implement, however, they are not able to handle sudden changes in vegetation growth, such as mowing events. On the other hand, hybrid methods, which utilize both temporal and spatial information, can achieve better results and are more capable of tackling the aforementioned issues. In the publication of [27], the authors evaluated and explored different parameterizations of five temporal reconstruction techniques. Even though the performance of some models was quite promising, the deviations in cloud-prone areas remained high.

The methods mentioned above focus on filling missing NDVI values using only the available cloud-free time series. However, utilizing ancillary data sources, such as SAR data, provides valuable information that can be correlated with optical-derived vegetation indices in order to tackle the problem. In recent years, the extensive adoption of Artificial Intelligence (AI) has led to a rise in the utilization of Machine Learning (ML) approaches for gap-filling [28, 12]. These approaches have shown promising performance across various land covers, including crops, grasslands, and forests. Unlike empirical models, which rely solely on initial hyperparameters and thresholds, these fully data-driven approaches require a large number of annotated training and validation samples to achieve high performance and ensure transferability and generalization.

In literature, one can find many studies on the joint exploitation of Sentinel-1 and Sentinel-2 observations. Standard ML regression routines, such as random forest, support vector machines or gaussian processes have been applied to capture the correlations between the different sources and generate optical data, based exclusively on SAR observations [29, 30]. How-

ever, these approaches do not consider the temporal information of the input data and have proven to be very sensitive to the initial hyperparameter selection, depending on the type of vegetation cover and area characteristics, which challenges their generalization and robustness.

The recent advancement in Deep Learning (DL), combined with increased computational capacities and the availability of open-access large datasets, paved the way for the successful adoption of fully automated data-driven approaches. Several works have been published that use CNN or Generative Adversarial Neural Networks (GANs) to exploit spatial characteristics and transform single date SAR images into equivalent optical ones [31, 32]. However, these approaches do not consider the dimension of time either, which is valuable information for crop monitoring, and usually have high computational complexity. On the other hand, RNNs are considered ideal for time series estimation because they are able to track temporal dependencies. Several architectures have been developed to exploit spatio-temporal data and enhance the prediction performance [33, 34]. Apart from RNNs, similar architectures can also effectively handle the cloud coverage issue, such as the one presented by [35].

In recent years, deep learning techniques that incorporate the temporal dimension have been effectively used for reconstructing optical vegetation indices using only SAR data. In [24], the authors propose the MCNN-seq framework which is a combination of a CNN and an LSTM layer. The CNN layer is used to reduce the impact of input noise and the LSTM layer, with an additional attention mechanism, addresses the problem of long time series to capture long-term dependencies in the data. However, despite this promising

architecture, its generalization capability should be further assessed, since only a small number of crop classes and a limited geographical extent were evaluated.

In [12] the authors propose a more sophisticated deep RNN design named SenRVM. This design involves the in-parallel processing of both descending and ascending orbits of Sentinel-1 SAR and coherence time series along with several auxiliary information, such as topographic, climatic and precipitation data. The approach’s capabilities are demonstrated through evaluation on three main vegetation types (grasslands, crops and forests) across two areas in France. The results suggest a satisfactory overall performance and emphasize its potential for generalization to large geographical areas. However, scaling up this methodology to the national level is difficult due to the challenge of acquiring the necessary auxiliary data and the time-consuming estimation of coherence coefficients. Nevertheless, for grasslands, the study found that ancillary information did not contribute significantly.

Recently, [11] applied a Transformer Temporal-Spatial Model (TTSM) on a megapixel spatial scale (i.e., 1M pixels), which exhibited quite promising scores and outperformed other deep learning solutions, such as LSTM, CNN/LSTM and LSTM with attention. Here, the authors utilized a transfer learning approach to test their model on two neighboring areas in China. The one area was used for training, and the other was used for testing on the reconstruction of missing images for two vegetation types (crops and forests). Although the results are promising, it’s worth noting that the areas tested are geographically close to each other and share similar land cover characteristics.

Overall, the aforementioned solutions focus on the general problem of reconstructing NDVI using SAR data for multiple land cover types. However, to the best of our knowledge, no studies have explicitly addressed the impact of cloudy images on the detection of mowing events in grasslands.

Grassland monitoring with remote sensing data has been widely studied. In order to detect grassland mowing, optical indices have been linked with interferometric SAR coherence of X and C bands [36]. However, confounding factors such as grazing events, farming activities, land factors and meteorological conditions can affect the accuracy of the results [37]. Combining optical and radar data can enable the tracking of sudden events and mapping of grassland use intensity [38]. Several current methods use fixed thresholds after parameters calibration, leading to model instabilities, in terms of performance [12]. The rule-based Sen4CAP algorithm [39] that uses both Sentinel-1 and Sentinel-2 time series was evaluated on six sites across Europe, achieving an overall accuracy of 69%. However, individual metrics on each area varied greatly (up to 30%).

Several studies have used machine learning for mowing event detection. In particular, [40] applied a deep learning model on sliding-windows of Sentinel-1/2 and Landsat 8 time series data for three consecutive years (2017-2019) in three regions of Germany. However, the study identified limitations, such as the interpolation of optical data to Sentinel-1 intervals, which may lead to the omission of events. [41] developed a CNN-based algorithm to quantify land-use intensity over grasslands across Germany using Sentinel-2 NDVI time series. Finally, [42] explored machine learning potentials within a two-step transferable approach on initial optical time series gap-filling and a subse-

quent mowing event classification that combines optical, SAR, and weather data.

3. Materials

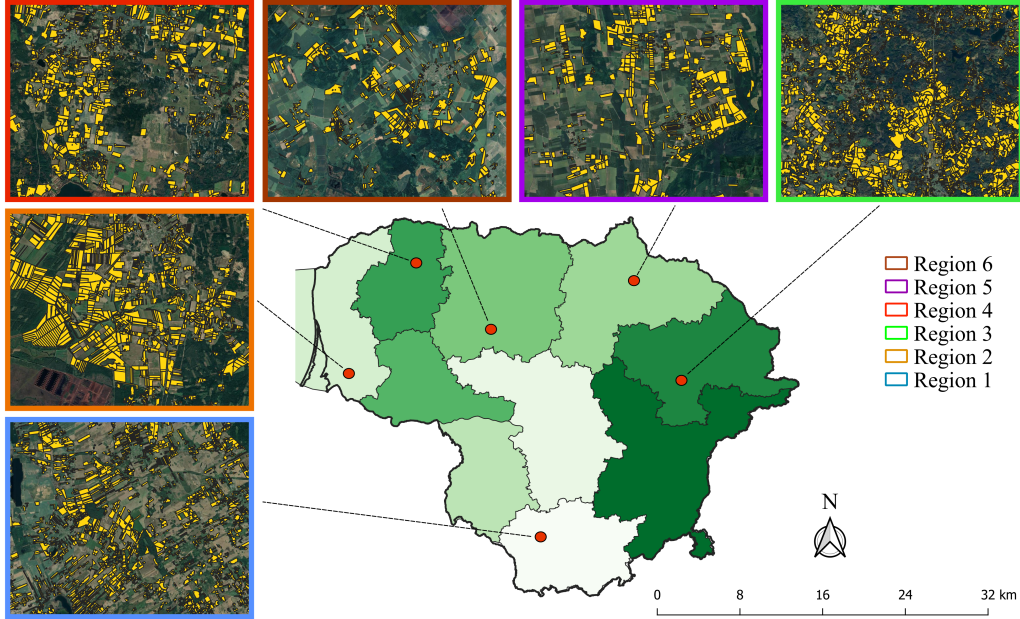


Fig. 1. Study sites in Lithuania.

3.1. Study area

Lithuania (Fig. 1) is located in Northeastern Europe and covers an area of 65,300 km². Its temperate climate is influenced by both maritime and continental factors, and it is primarily defined as humid continental under the Köppen classification scheme. However, a small coastal zone adjacent to the Baltic Sea can be considered oceanic. It is mainly characterized by cold temperatures, frequent rainfalls, and snowy winters. As a result, four

climatic regions have been identified: Coastal, Samogitian, Middle Lowlands, and Southeastern Highlands [43].

Grasslands are the most prevalent crop types and are spread equally across the country. They are divided into two main categories: permanent and temporary grasslands. Permanent are mostly perennial pastures and meadows, or other natural/semi-natural grassland parcels of the same land use for more than five years. On the other hand, temporary grasslands are the cases of newly updated grassland usage, of less than five years. In Lithuania, CAP requires farmers to perform at least one agricultural activity (mowing or grazing), usually until 1st of August of every cultivation period.

In this study, six distinct sites were selected based on their different agro-climatic and morphological characteristics as determined by Lithuania's climatic region map and the distribution of grassland cultivation.

Region 1 is located in the county of Alytus (southern Lithuania) at the center of the Dzūkija region that is mostly covered with pine forests. Despite being watered by the Nemunas river, this area is unsuitable for agricultural activities due to the poor quality of the soil, which is mostly sandy. Regions 3 and 5 are located around the counties of Utena and Panevėžys, respectively, in the northeast part of the country and inside the region of Aukštaitija, which contains more urban elements than the rest. In the Samogitia region, an area in the northwestern Lithuania with many lakes and intense agricultural activity, we find Regions 4 and 6, near the counties of Telšiai and Šiauliai, respectively. Finally, Region 2 is in the county of Klaipėda, located in the western part of the country. Its climate is highly influenced by the Baltic Sea, with very frequent storms, as well as snowfalls and gales during

winter. Table 1 contains the number of grassland parcels and their average size for each study site. The average size of grassland parcels in entire country is over 1 ha (see the respective Figure S1 in [Appendix A](#)), which is substantial bigger in comparison to other European countries. However, there are a few cases with size less than 0.1 ha, which results to mixed information within the Sentinel-2 pixels and have been eliminated from our study.

Table 1

Number of grasslands parcels and their respective average size in hectares (ha) for the six study regions.

Region	# parcels	Avg. parcel size (ha)
Region 1 (Alytus)	10,426	1.33
Region 2 (Klaipėda)	7,497	2.35
Region 3 (Utena)	11,181	1.75
Region 4 (Telšiai)	9,075	1.82
Region 5 (Panevėžys)	2,760	2.58
Region 6 (Šiauliai)	4,287	1.80

3.2. Sentinel Data

In this study, we utilized both Sentinel-1 and Sentinel-2 satellite imagery. We obtained Sentinel-1 GRD and SLC, as well as Sentinel-2 L1C data for the year 2020 from the CreoDIAS data repository. It is worth noting that the data acquisition period is before December 2021, prior to the instrument electronics power supply anomaly occurred on Sentinel-1B [\[44\]](#). As a result,

the revisit time for the radar data is 6 days.

The study areas are spread evenly throughout the Lithuania, with multiple orbits intersecting with each other to cover the regions of interest. From the total of 14 available Sentinel-2 tiles, 8 (i.e., 34UEG, 34UFG, 34UFF, 34VEH, 35ULA, 35ULB, 35UMB and 35VLC) intersect with the respective study sites. Moreover, two Sentinel-1 relative orbits were selected, namely 58 and 131, which in combination cover the entire country of Lithuania and guarantees consistent acquisition geometry of the respective time series per study site. Additionally, these specific orbits are acquired in the afternoon, which is crucial for grassland monitoring since morning dew can cause unexpected decrease of coherence on both mowed and unmowed parcels [37].

3.2.1. Data Processing

A time series of Sentinel-2 images was collected between April 1st and September 30th, 2020. The images were atmospherically corrected using the sen2Cor software [45], transforming them from Top of Atmosphere (TOA) Level 1C to Bottom of Atmosphere (BOA) Level 2A products. The resulting products also contain the Scene Classification Layer (SCL), which includes a pixel classification map for clouds, cloud shadows, vegetation, and other features. The images were then reprojected and clipped to the areas of interest. Our focus is primarily on the calculation of NDVI (see Table 2), which uses the B04 and B08 bands representing the red and near-infrared wavelengths, respectively. Both bands have a spatial resolution of 10 m.

We used Level-1 Ground-Range-Detected (GRD) products from Sentinel-1 imagery in Interferometric Wide (IW) swath mode to generate backscatter coefficient (σ_0) and Single-Look-Complex (SLC) products, which were used

to compute the interferometric coherence coefficients. The GRD data pre-processing was performed using the snappy library, which included clipping to the area of interest, radiometric calibration, speckle filtering with the Refined Lee Filter (RLF), terrain correction using Shuttle Radar Topography Mission (SRTM) 10-m, and conversion of backscatter coefficient into decibels (dB). For the SLC products, we applied TOPS Split to select only the essential bursts for analysis. The next step was to retrieve and apply orbit auxiliary data that contained information on the satellite’s position during SAR data acquisition. Then, the Sentinel-1 Back-Geocoding process was used to co-register the split products based on updated orbit information and a Digital Elevation Model (DEM). Finally, we estimated the coherence between the reference and secondary images, taking into account any differences in imaging conditions, which provided information on any changes or movements that may have occurred between the two acquisitions. All coefficients were computed in VV and VH polarization modes.

Furthermore, apart from the backscatter and coherence coefficients (in VV and VH polarization), we also calculated four products based on combinations of them, namely the mixed coherence, the Radar Vegetation Index (RVI), the backscatter ratio and the backscatter cross-ratio. In Table 2, we summarize the list of all features extracted from Sentinel-1 and Sentinel-2 for the development of this study.

To handle the large amount of data efficiently, we utilized the Agriculture monitoring Data Cube (ADC) developed by [46]. The acquisition dates for the Sentinel satellites varied by region, so we brought all data components into a common temporal framework based on the acquisition dates

Table 2

Features used in this study and their relevant description or formula. σ_0 refers to the backscatter coefficient and coh is an abbreviation for coherence.

Feature	Description
σ_0	VV and VH bands from Sentinel-1 GRD
coherence	VV and VH bands from Sentinel-1 SLC
σ_0 ratio	$\frac{\sigma_0 VV}{\sigma_0 VH}$
σ_0 cross-ratio	$\sigma_0 VH - \sigma_0 VV$
mixed coherence	$\sqrt{\text{coh}_{VV} \cdot \text{coh}_{VH}}$
RVI	$\frac{4 \cdot \sigma_0 VH}{\sigma_0 VH + \sigma_0 VV}$
NDVI	$\frac{\text{NIR} - \text{RED}}{\text{NIR} + \text{RED}}$

of Sentinel-1 data, in each area of interest, to ensure consistency in our dataset. Since most regions were covered by relative orbit 131, we used its acquisition dates as a reference for the common temporal framework. We then shifted all other measurements from Sentinel-2 and Sentinel-1 (orbit 58) satellites to the closest Sentinel-1 date of the 131 orbit. As a result, the final dataset consists of time series with a 6-day time step from April 9th, 2020 until September 24th, 2020, containing 29 individual timestamps. We shifted Sentinel-2 cloud-free timestamps to the closest date of reference only if there was a 3-day distance between them. Otherwise, we denoted the corresponding timestamps as empty (i.e., with NaN values).

We used the same interpolation method to fill missing values for pixels that had been masked out due to clouds from the SCL product of the sen2Cor

software. However, these cloud masks are not always accurate, especially in cases of cloud shadows, thin clouds, or pixels adjacent to clouds, which cause an underestimation of the NDVI value that can potentially lead to incorrect detection of mowing events [47]. To address this issue, we implemented Algorithm 1, which is a threshold-based module, and applied it to each pixel’s time series. The aim of this module is to remove cases of a sudden drop in NDVI (parameter α) followed by a relevant sudden increase (parameter β) between two successive time-steps (Fig. 2). In our case, we configured both α and β threshold parameters for the sudden drop and relevant increase to 0.15. This deliberate choice of a relatively high threshold, minimizes the overall number of cases that are removed, ensuring that only certain noisy timestamps are filtered out. Additionally, we examined the difference between the NDVI values in the timestamps before and after the examined one, to prevent removal of cases caused by gradual NDVI decline due to grassland senescence. This difference should be at least -0.05 (parameter γ). An equivalent approach has been developed by [48] using NDVI triplets and the rhombus equation for the identification of outlier cases. Similarly, in the recent study of [49] a gradient boosting algorithm is trained to detect false positive mowing predictions caused by missed clouds.

3.2.2. Annotated data

One of the main objectives of this study is to enhance event detection algorithms by utilizing artificially generated NDVI time series. However, in order to evaluate the effectiveness of these algorithms, labeled data are necessary, which are typically collected through expensive and time-consuming in-situ campaigns. As conducting such campaigns on a large scale is not

Algorithm 1 Identification and removal of outlier cases

procedure OUTLIERS DETECTION(α, β, γ)

Read series of raw cloud-free NDVI values: S

$T = \text{len}(S)$

for $t \in T$ **do**

$$C_\alpha \rightarrow \frac{S(t) - S(t-1)}{DoY(t) - DoY(t-1)}$$

$$C_\beta \rightarrow \frac{S(t+1) - S(t)}{DoY(t+1) - DoY(t)}$$

$$C_\gamma \rightarrow S(t+1) - S(t-1)$$

if ($C_\alpha \geq \alpha$ **and** $C_\beta \geq \beta$ **and** $C_\gamma \geq \gamma$) **then**

$S_t \rightarrow \text{NaN}$

end if

end for

end procedure

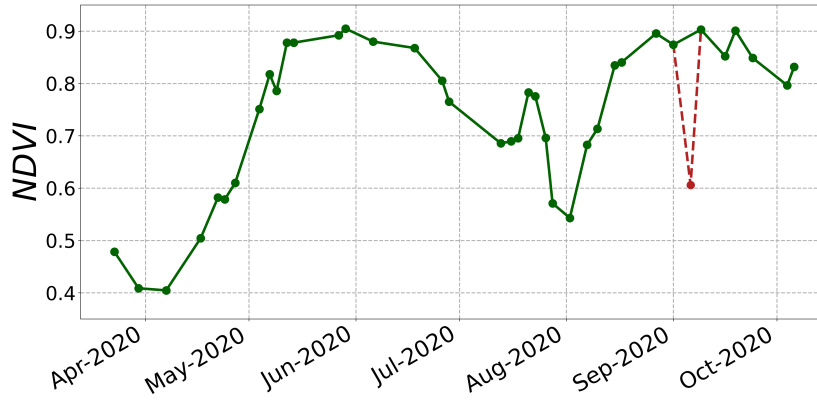


Fig. 2. Example of NDVI time series outlier removal. The red dashed line shows the raw NDVI time series (i.e., including noise), and the green line illustrates the NDVI after filtering out potential cloudy measurements that remained following the cloud masking step.

feasible, we employed a photo-interpretation process, carried out by three experts, to annotate data for our study.

To streamline the assessment process, we utilized validation data from the Lithuanian Paying Agency (NPA) as a starting point within the regions of interest. The parcels selected were compliant with national mowing regulations, meaning that at least one agricultural event had occurred by August 1st, although the exact timing of this event was unknown. Moreover, for the photo-interpretation process we selected parcels with minimal cloud coverage during the inference period. This approach minimized the risk of overlooking cases that might have gone undetected due to persistent cloud cover, as no extended gaps beyond a few days were observed in these timestamps.

The photo-interpretation process was carried out by three experts that used multi-temporal Sentinel-1 and Sentinel-2 images as reference. Since Sentinel satellites do not offer daily observations, the labeling process involved identifying the closest timestamps before and after a grassland event took place, from early April to late September. Each expert independently assigned labels on the acquisition dates of Sentinel-2, indicating the date before and after a grassland event has occurred. The samples were distributed evenly across the six sites to ensure reliable model optimization and results assessment. Since SAR coefficients are sensitive to changes in the canopy of grasslands, the photo-interpretation analysis additionally incorporates Sentinel-1 data. Steep changes between successive images may showcase the occurrence of a potential grassland event. For this reason, true color and false color (B08-B04-B03) composites of Sentinel-2 time series have been found to be particularly useful in identifying the presence of an event

(Fig. 3).

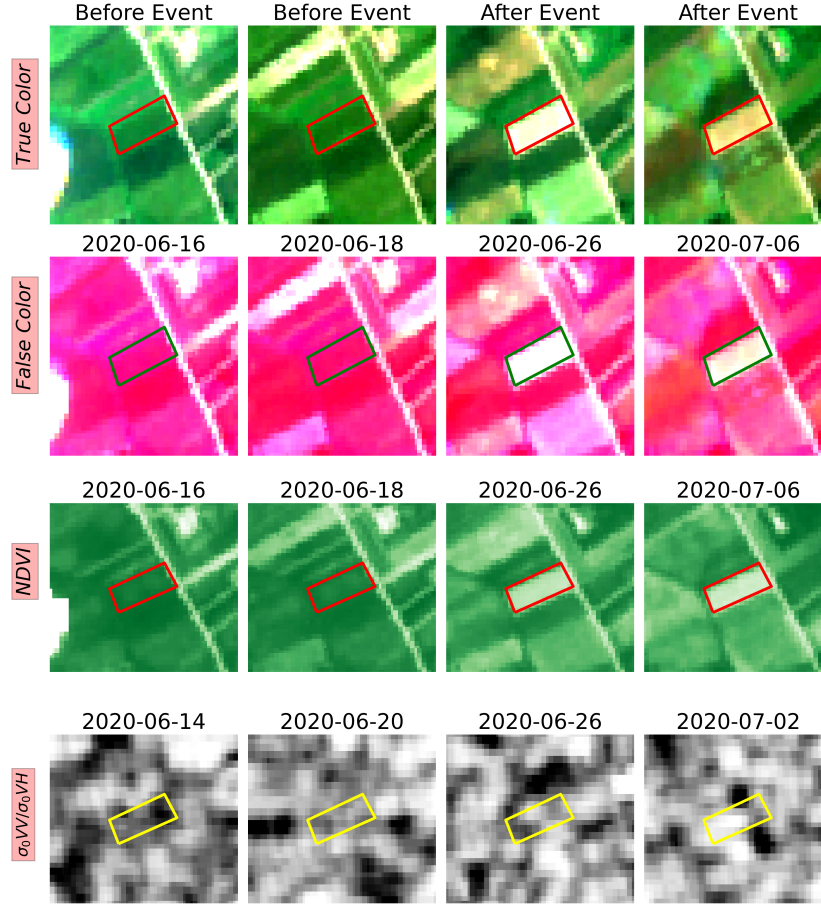


Fig. 3. Time series of Sentinel-1 and Sentinel-2 images for detecting a grassland mowing event. An event can be observed between June 18th and June 26th. The integration of Sentinel-1 imagery further narrows down the detection period of the event.

Then, the examination of NDVI and SAR multi-temporal signatures were used to guide the decision of the photo-interpreter. Their decision was dictated by the fact that NDVI gets much lower values after an event (at least a decrease of 0.1), while SAR coefficients acts the opposite (Rules 1-2). Secondly, an event must take place on compact dense areas and not scattered

spots inside grassland parcels (Rule 3). If all the above are met, the final decision lies on the consequent values of NDVI (Rule 4). Cases where NDVI does not increase shortly (usually up to 15 days) after the potential event are excluded and are not considered as valid events. This behaviour many times resemble harvest events, and thus such cases may have been wrongly characterized as grasslands.

Following the visual assessments by the experts, final labels were determined through a majority voting system. Specifically, when two experts agreed on a label, this was considered the correct one. The agreement percentage between Expert 1 and 2 was 88%, between Expert 1 and 3 was 93%, and between Expert 2 and 3 was 86%. However, in around 5% of all cases, a disagreement emerged among all three experts, necessitating a collective decision to determine the final label.

The procedure was applied in all six study sites and the final dataset includes 803 parcels, which correspond to 287,281 individual pixels (see Table 3). In this dataset, 650 cases had one mowing event, 99 cases multiple mowing events, and 54 cases showed no evidence of mowing. Notably, a significant amount of the identified mowing events occurred during the June and early July (refer on Fig. S2 in the Appendix A for details).

4. Methods

4.1. Cloud coverage distribution

The study regions are characterized by unique cloud coverage profiles. Fig. 4 visualizes the percentage of grassland parcels affected by clouds on each date and each study region. We observe significantly lower cloud cov-

Table 3

Number of parcels and pixels annotated for mowing events for each region.

Region	# parcels	# pixels
Region 1	274	64,141
Region 2	189	106,556
Region 3	98	33,065
Region 4	91	39,254
Region 5	79	23,639
Region 6	72	20,626
Total	803	287,281

erage during summer months (from June to August), when most of mowing events occur. However, there are still cases that grassland activity is not observed or not identified soon enough due to clouds.

We determined the cloud coverage for each grassland parcel by calculating the ratio of cloudy Sentinel-2 observations to the total of acquisition dates. The mean cloud coverage for the entire dataset is approximately 45%. To ensure higher quality ground truth information, we worked with pixel time series and selected only the densest ones. Specifically, we excluded cases that had i) more than one successive missing value during June and July, ii) more than 3 missing values in total during June and July, iii) more than two consecutive missing values during the rest of the assessed period, and iv) an overall cloud coverage higher than 35%. This approach helps ensure that we did not omit any mowing events. Finally, given that in dense time series

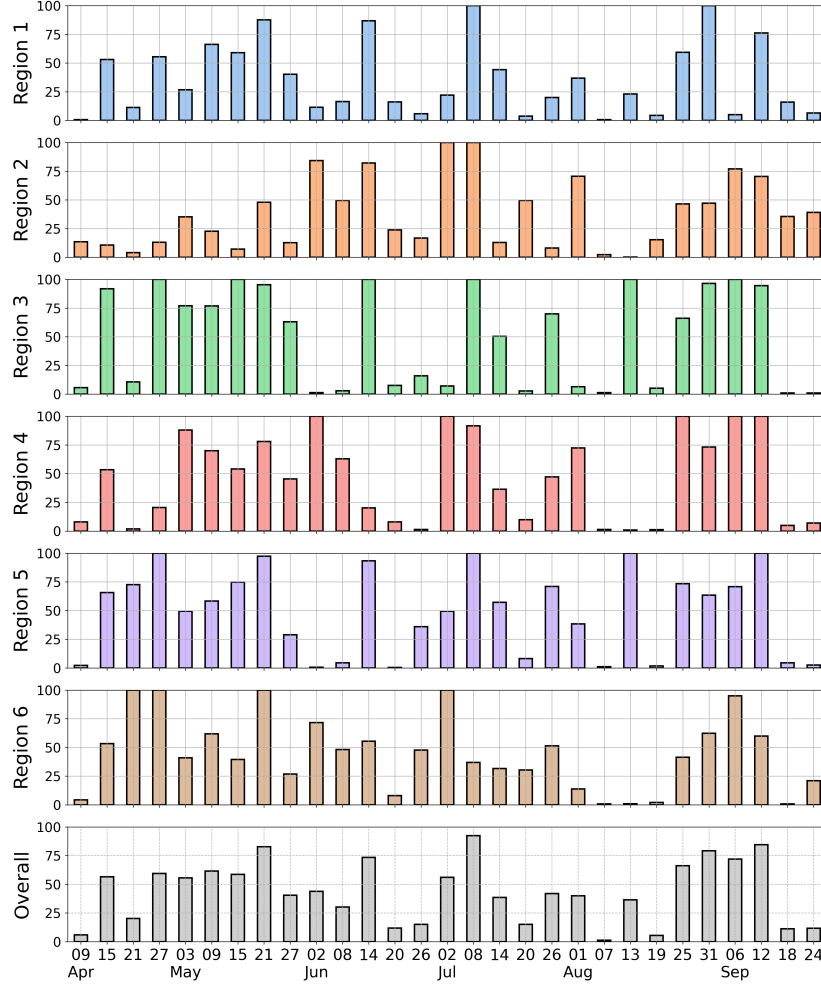


Fig. 4. The percentage of grassland parcels affected by clouds on each reference date. The colors in this figure correspond to the colors used for each study area, as these are depicted in Fig. 1.

simple temporal interpolation methodologies are able to effectively fill the short-term gaps, we used the Akima method [50] to generate the full target NDVI time series.

4.2. Artificial masking

To train and validate our methodology, we used artificially generated cloud masks, which were used to mask out specific timestamps in the dense NDVI time series. For each region, we collected a set of binary time series indicating the presence or absence of clouds, based on the actual cloud coverage distribution in the corresponding area. Subsequently, we used a bootstrapping procedure to assign a random cloud mask to each NDVI time series. Further, we ensured consistency by applying the same mask to all pixels within the same field boundaries. This approach ensured standardization across various parcels and maintained the alignment with the typical cloud coverage distribution in each region. An example of the NDVI values of a pixel after applying a cloud mask is shown in Fig. 5.

4.3. Model training and architecture

The proposed deep learning Sentinel-1/2 Fusion (SF) methodology is composed of sequential CNN and LSTM blocks (Fig. 6). It is a supervised-learning neural network architecture that aims to extract full NDVI time series from Sentinel-1 time series and the available cloud-free Sentinel-2 observations. This architecture is based on the one proposed by [24], with the main difference being the inclusion of masked NDVI time series in the input feature space.

4.3.1. CNN block

‘The CNN block (CB) is used to reduce the impact of noise in the input and extract meaningful features for the subsequent layers. The block consists of N parallel and independent between them, one-dimensional convolutional

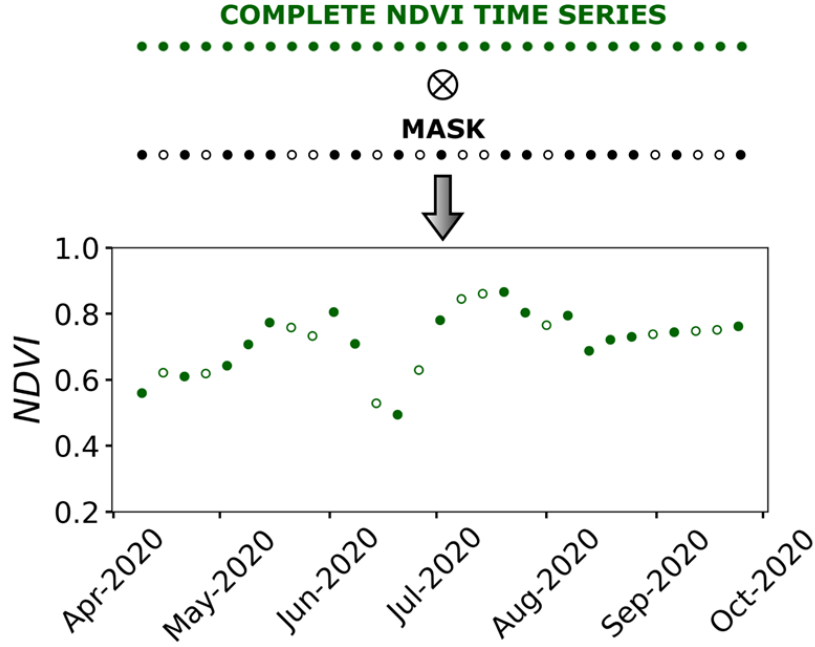


Fig. 5. NDVI time series with artificial cloud masking. The green dots on top of the plot show the complete NDVI time series for a pixel post-processing, with the black and white dots directly beneath representing a simulated cloud mask. In the scatter plot, the NDVI time series after the application of the artificial mask is displayed. Non-filled green dots indicate values that have been masked and are treated as missing data, while the filled green dots denote the ground truth.

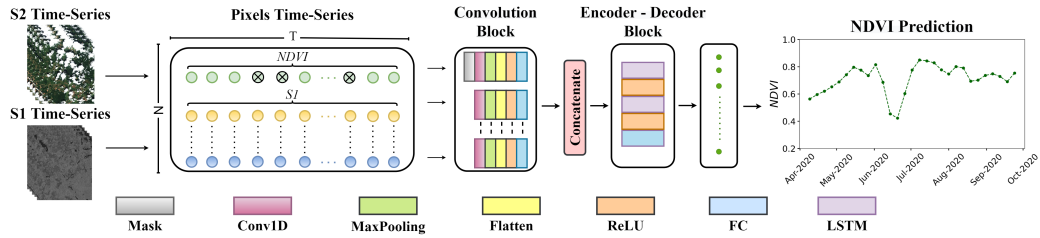


Fig. 6. Overview of the model's architecture for reconstructing continuous NDVI time series with a fixed 6-day time step using SAR data and the available NDVI values.

branches (Conv1D), where N is the number of input channels. Each Conv1D branch is followed by max-pooling layers to reduce the dimensionality of the output. Following this, a non-linear Rectified Linear Unit (ReLU) activation function has been applied to transform negative values into zeros. The resulting feature maps are passed to a fully-connected layer to provide the final embeddings into the subsequent LSTM blocks. In the case of NDVI branch, a masking layer is added as the first layer in order to filter out masked NDVI inputs, which account for cloud presence. This strategy ensures that the network considers the cloudy NDVI timestamps as hidden and tries to reconstruct the complete NDVI time series based on the available cloud-free observations and the additional SAR data. The output of each Conv1D branch is a collection of feature maps that represent various characteristics of the input data. These feature maps are subsequently concatenated along the channel dimension and then forwarded to the encoder-decoder block.

4.3.2. Encoder-decoder block

RNNs are commonly used to analyze sequential data, as they can effectively identify patterns and dependencies between consecutive time steps. One of their key benefits is the capacity to retain information from previous time steps and use it to predict the current state, while sharing parameters across all time steps. To handle variable-length inputs and outputs, we have employed an encoder-decoder architecture with Bi-directional LSTM modules. These modules process input sequences in both forward and backward directions, allowing them to capture context from past and future time steps. The final NDVI time series is produced by a fully-connected layer that receives the output of the encoder-decoder block (EDB). The EDB consists of

LSTM modules that perform the following operations:

$$f_t = \sigma(W_f[h_{t-1}, x_t] + b_f) \quad (1)$$

$$i_t = \sigma(W_i[h_{t-1}, x_t] + b_i) \quad (2)$$

$$\tilde{C}_t = \tanh(W_C[h_{t-1}, x_t] + b_C) \quad (3)$$

$$C_t = f_t * C_{t-1} + i_t * \tilde{C}_t \quad (4)$$

$$o_t = \sigma(W_o[h_{t-1}, x_t] + b_o) \quad (5)$$

$$h_t = o_t * \tanh(C_t) \quad (6)$$

where x_t is the input at time t , h_{t-1} is the previous hidden state, c_{t-1} is the previous cell state, i_t is the input gate, f_t is the forget gate, o_t is the output gate, c_t is the cell state at time t , and h_t is the hidden state at time t . The weights and biases of the LSTM are represented by W and b , respectively. The sigmoid function is denoted by σ , and the hyperbolic tangent function by \tanh .

4.3.3. Model training

The CB includes an independent branch for each input layer. Each branch comprises two Conv1D layers with filter sizes of 8 and 16, both using a kernel size equal to 3. These are followed by a max pooling layer with a pool size of 3 (without striding), and finally, two fully-connected layers, with 32 and 16 units, respectively. To determine the optimal configuration, we conducted experiments with various parameter sets.

The EDB was constructed using LSTM units with a 16-unit latent space. For the training, we employed the Adam optimizer, together with the Mean

Squared Error (MSE) loss function. The latter, will allow us to effectively penalize significant errors that might arise from substantial discrepancies between predicted and target values, particularly when dealing with noisy data, such as preserved cloudy measurements. The initial learning rate was set to 0.005, and the batch size to 256. The training procedure included early stopping, which would terminate the process if the loss function did not improve after three consecutive epochs, with a maximum of 30 epochs to prevent overfitting.

In addition, incorporating the NDVI time series as both input and target can result in the model being prone to overfitting to those specific values. To address this issue and force the network to give higher attention on masked timestamps, we have used temporal weighting for each input sample. Masked NDVI values were assigned a training weight parameter of w_α , while non-masked values were given a smaller weight parameter of w_β . These parameters were set to be 0.75 and 0.25 respectively since they provided the optimal results. Additionally, as we utilized interpolation to produce a complete target time series, the values in timestamps that are not actual measurements and have been derived from the interpolation are assigned a weight of 0.

Finally, to ensure an unbiased evaluation of both the NDVI reconstruction and the grassland event detection tasks, we selected the training set from randomly selected parcels across the study sites. For the NDVI reconstruction assessment, we also selected random pixels from parcels across the test sites. To avoid any bias in the subsequent evaluation of mowing events, we excluded all the pixels within the parcels that were annotated through the photo-interpretation process (Section 3.2.2) from the training set. Table

4 shows the numbers of parcels and pixels of the training and test sets in the six regions, for the NDVI reconstruction task.

Table 4

Number of training and inference pixels and parcels for each region.

Region	# training pixels (# parcels)	# inference pixels (# parcels)
Region 1	408,132 (2002)	86,747 (367)
Region 2	184,452 (564)	140,242 (253)
Region 3	68,180 (364)	36,715 (108)
Region 4	158,419 (737)	47,785 (107)
Region 5	49,377 (199)	25,502 (86)
Region 6	114,742 (451)	28,307 (101)
Total	983,302 (4317)	365,298 (1022)

The experiments were conducted on a system with an Intel Core i7-9700 CPU (8 cores, 3.0 GHz), 16GB of RAM, and an NVIDIA GeForce GTX 1660 GPU (6GB GDDR5 memory). On this setup, the average training time per epoch for a training dataset of 983,302 instances was approximately 31.8 seconds.

4.4. Event detection

Mowing Detection Algorithm I (MDA I) is the algorithm developed by [39], in the context of Sen4CAP project. Its Sentinel-2 component of the processing chain for mowing detection searches for significant and sharp drops between consecutive NDVI cloud-free observations, surpassing a predefined threshold. This algorithm is considered a solid method for mowing event

detection and similar methodologies have been widely used the past years. The evaluation of its performance across several European countries for 2019 demonstrated f1-score of 79% over 150 parcels in the Netherlands. However, when evaluated on 118 cases in Lithuania, it showed a notably lower f1-score of 60%, mainly due to a significantly reduced precision of 49%.

Mowing Detection Algorithm II (MDA II) is the algorithm proposed by [51]. They suggest to consider the residuals of the assessed vegetation index values from an interpolated time series formulated based on the seasonal peak timestamps that represent the ideal growing season curve. This algorithm achieved an overall f1-score of 67% on 180 grassland parcels in Germany for 2020. The repository for their implementation was collected and cloned as a user-defined function in the FORCE processing environment¹.

Both these methods, while not perfect, presented quite satisfactory results in our dataset. Nonetheless, we want to assess whether using SF to generate artificial cloud-free NDVI time series, we can improve the mowing event detection accuracy. Thus, we use these methods as baseline, since they are highly dependent on the NDVI information and can directly highlight the importance of the proposed methodology.

Deep Learning Mowing Detection Algorithm (CNN-RNN): Apart from the fusion task, we utilize the SF architecture as an event detection algorithm. However, for the aim of this task, we keep only the NDVI branch at the input of the network since the purpose now is to evaluate the mowing detection accuracy given the full NDVI time series provided. Furthermore,

¹<https://github.com/davidfrantz/force-udf/tree/main/python/ts/mowingDetection>

we replaced the existing activation function at the end of the output layer with a sigmoid one, in order to quantitatively assess the probability of an event occurring at each distinct timestamp. For the training of the model we utilized the annotated labels that were derived through photo-interpretation, as mentioned in Section 3.2.2. For this purpose, we created binary series of 0s and 1s with a size equal to the length of the time series (in our case, 29). In this binary representation, the value 1 corresponds to the closest timestamp to the annotated mowing event. This labeling format allows for the model to learn intricate temporal patterns, enabling it to offer not just event detection but also a probability estimation for the likelihood of an event occurring at each timestamp within the extensive range of evaluated dates. This dual-purpose application of the SF architecture will showcase its versatility in addressing complex tasks beyond NDVI reconstruction, highlighting its potential as an effective event detection algorithm, too. It’s worth noting that while we acknowledge the potential contribution of SAR branches to the model’s accuracy, their inclusion in this model configuration would introduce an unfair advantage. Our objective here is to assess and quantify the unique contributions of the same optical features through different models, ensuring a fair and robust evaluation.

5. Results

In this section we evaluated the SF model’s performance in cloud gap-filling. We compared its performance with other common interpolation methods, namely Linear Interpolation (LI), Akima Interpolation (AI) and Quadratic Interpolation (QI). Additionally, we assessed the effect of missing NDVI im-

ages on the detection of grassland events and the ability of the SF model to alleviate this problem.

5.1. Gap-filling model performance

This section evaluates the performance of the SF model on the six grassland regions. For the evaluation we used the metrics of Mean Absolute Error (MAE) (Eq. 7) and coefficient of determination (R^2) (Eq. 8), considering all available time steps with a cloud-free NDVI value.

$$MAE = \frac{1}{n} \sum_{i=1}^n |y_i - \hat{y}_i| \quad (7)$$

$$R^2 = 1 - \frac{\sum_{i=1}^n (y_i - \hat{y}_i)^2}{\sum_{i=1}^n (y_i - \bar{y})^2} \quad (8)$$

where \hat{y}_i is the predicted value of the i -th pixel, y_i is the corresponding true value for n total pixels and $\bar{y} = \frac{1}{n} \sum_{i=1}^n y_i$.

In Figure 7, we present scatter plots for each of the six study regions. Notably, we have noted a strong correlation between the ground truth and the predictions generated by the SF model. Region 5 stands out with relatively poorer performance, characterized by a MAE of 0.028 and a R^2 value of 0.88. This discrepancy can be attributed to the presence of relatively high cloud coverage and a limited number of training pixels from the area. However, when assessing the other regions, we did not find any statistically significant differences in performance. Collectively, the R^2 coefficient measures at 0.92, and the MAE is calculated at 0.024, which highlights on SF model's capacity in effectively generating missing NDVI values.

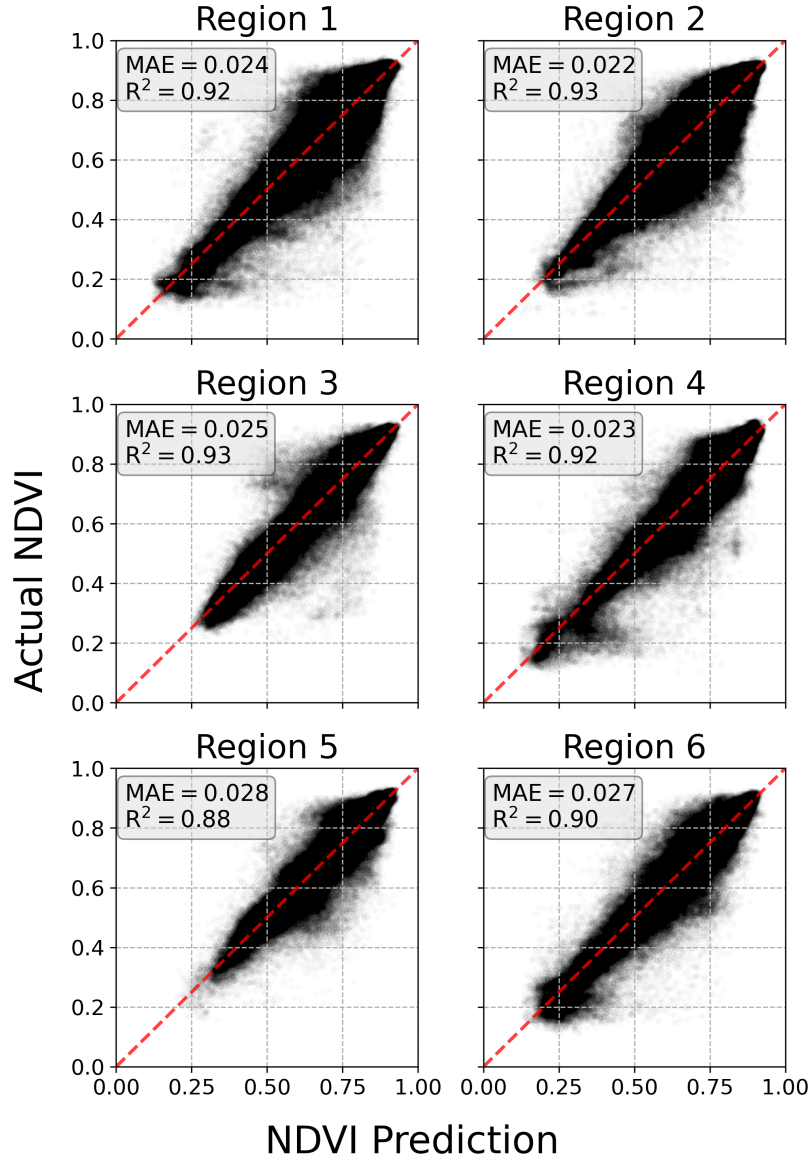


Fig. 7. Scatter plots between the actual NDVI values and the SF predictions for each study region.

Fig. 8 presents the distribution of MAE for the SF model and the three alternative interpolation methods. This analysis focuses on timestamps that

were intentionally masked in order to highlight the model’s ability to fill missing NDVI values. The SF model outperforms the temporal interpolation methods, with a mean MAE of 0.036 and a median of 0.032. In contrast, the AI and LI methods exhibit less favorable results, with average MAE values of 0.043 and 0.044, respectively. The QI method performs the poorest among the approaches, with an average MAE of 0.047 and a notably higher standard deviation.

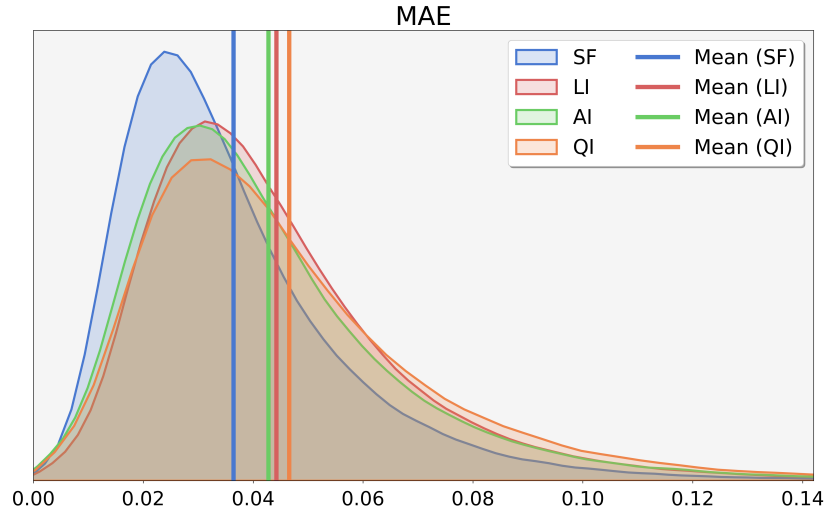


Fig. 8. The distribution of MAE, only on the masked timestamps, for the SF and the three interpolation methods (AI, LI, and QI).

For further details regarding cloud gap-filling performance across various parameters such as study site, date of inference, cloud coverage, and length of consecutive missing values, please refer on [Appendix A](#) Figures S4 to S7.

5.2. Event detection accuracy assessment

In this section, we evaluate the SF methodology’s contribution to the detection of grassland mowing events. We use event timestamps as labels

to assess the impact of the artificially created NDVI time series on the event detection task. We examined 803 unique grassland parcels across six regions, which correspond to 287,281 pixels, and derived from the photo-interpretation process (Section 3.2.2).

Our evaluation investigates how the SF model affects grassland event detection by comparing two rule-based methods outlined in Section 4.4. These methods depend exclusively on NDVI time series to identify substantial drops in their values. Consequently, they may exhibit limitations in detecting events, especially when consecutive cloudy observations are present. They provide a time range for each event, allowing us to compare it directly with the respective range obtained from photo-interpretation. Finally, we measure the detection accuracy and the ability to predict an event correctly using recall (Eq. 9) and precision metrics (Eq. 10), and their harmonic mean using the f1-score metric (Eq. 11). The predictions are aggregated and evaluated at the parcel level.

$$Recall = \frac{True\ Positive}{True\ Positive + False\ Negative} \quad (9)$$

$$Precision = \frac{True\ Positive}{True\ Positive + False\ Positive} \quad (10)$$

$$F_1 - Score = \frac{2 \cdot Precision \cdot Recall}{Precision + Recall} \quad (11)$$

A predicted event is deemed correct if its predicted date falls within twelve days (tolerance parameter) before or after the actual event, which is twice the size of the time series interval. Events falling outside this tolerance window are considered false positives. This approach helps mitigate issues arising

from the 6-day interpolation used for detection. This may cause events to shift from one timestamp to another, introducing challenges when reporting results, as it can impact the accuracy and alignment of detected events with their actual occurrences. Furthermore, while MAE is a common metric for evaluating mowing event detection algorithms, it is not considered applicable in our case since we lack the exact date of the mowing events. Our main purpose in this study is to assess how the implementation of the SF model for reconstructing missing NDVI values enhances mowing event detection by identifying cases that would have been missed otherwise. Nevertheless, in [Appendix A](#) (Tables S1-S3), we present the respective results for various evaluation approaches, which highlights the independence of the SF model on the criteria used to define a predicted event as correct.

Table 5 shows the results of MDA I and MDA II algorithms acquired from the different interpolation methods and time series without any interpolation applied. Both algorithms demonstrate similar performance, with slight variations depending on the interpolation methodology. As indicated in the table, all interpolation approaches exhibit a common tendency to slightly underestimate recall while significantly enhancing precision accuracy for both mowing detection algorithms, compared to using unprocessed time series data. This can be attributed on the interpolation capabilities to effectively eliminate numerous abrupt changes that often arise from noisy NDVI successive values by providing consistent timestamps with a 6-day gap between them. All in all, this behaviour decreases the total number of false detected mowing events (i.e., increased precision), reducing the number of some correctly identified cases though (i.e., reduced recall). In essence, these findings highlight the

compromise between precision and recall, emphasizing the role of interpolation methods in refining mowing event detection accuracy. Specifically, the SF provided NDVI time series, present the best results in both MDA I and MDA II, with the latter achieving the optimal f1-score equal to 0.84. For MDA I, recall presents lower values for all interpolation methods comparing the raw NDVI time series, while for MDA II, SF managed even to improve detection accuracy by almost 1% compared to raw time series. Furthermore, SF offers significantly higher precision (over 90%) for both MDA I and II, with a range of 19% to 24% improvement over the initial NDVI time series.

In Fig 9, we present f1-score categorized by cloud coverage percentage (ccp). We divided the groups using the mean ($\mu \simeq 0.4$) and standard deviation ($\sigma \simeq 0.1$) values of the cloud coverage distribution, which resembled a normal distribution. Based on this statistical analysis, we constructed four distinct categories accordingly: $ccp < \mu - \sigma$ (101 cases), $\mu - \sigma \leq ccp < \mu$ (252 cases), $\mu \leq ccp < \mu + \sigma$ (291 cases), $ccp \geq \mu + \sigma$ (159 cases). The figure reveals that SF's delivers consistently superior performance across the various cloud coverage scenarios, which highlights its robustness against any cloud coverage situation. This is becoming more evident in cases with very high cloud coverage percentage. This can be attributed to SF's ability to handle cases resembling extended cloud coverage, which often obscure mowing events. The NDVI time series constructed based on SAR data excels in recovering such challenging cases, resulting in better performance.

Fig. 10 illustrates the recall, precision, and f1-score obtained from both MDA I and MDA II across each of the study regions. Once again, the results obtained from MDA II exhibit a slight improvement over MDA I. Notably,

Table 5

Comparative analysis of MDA I and MDA II algorithms for grassland event detection using i) no interpolation, ii) Linear Interpolation (LI), iii) Akima Interpolation (AI) iv) Quadratic Interpolation (QI), and v) the SF model.

Algorithm	Interpolation	Recall	Precision	F1-score
MDA I	-	0.755	0.717	0.736
	LI	0.719	0.800	0.757
	AI	0.712	0.803	0.755
	QI	0.732	0.800	0.765
	SF	0.749	0.928	0.829
MDA II	-	0.762	0.730	0.746
	LI	0.635	0.843	0.724
	AI	0.696	0.857	0.768
	QI	0.707	0.859	0.776
	SF	0.770	0.923	0.840

Region 3 stands out with optimal results with precision values close to 1 and very high recall rates, which results to f1-score surpassing 0.9 for both MDAs. Similar behavior exhibit Regions 4 and 5, too. On the other hand, the rest of the Regions present worse performance, with and f1-score around 0.80. It is important to highlight that overall, precision can reach significantly high values, occasionally approaching 1, when we utilize the NDVI time series constructed with the SF model. This effect can be attributed to SF model's ability to correct cloudy observations and thus prevent the MDAs to

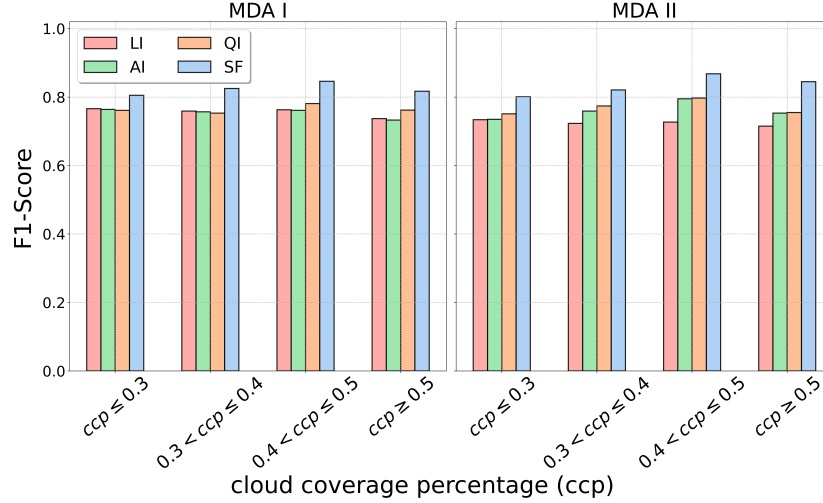


Fig. 9. F1-score for mowing event detection and for different cloud coverage percentage (ccp) scenarios. For further analysis, these results are detailed in Table S5 in [Appendix A](#).

incorrectly identify these cases as mowing events.

In Fig. 11, a scatter plot is presented that compares the ground truth and predicted values using MDA II, which has proved to be slightly more robust than MDA I. Only absolute differences less than 12 days are considered accurate, as larger gaps are deemed too significant. The size of each point indicates the number of observations on this reference day. The plot shows a linear relationship between the measures, with an R^2 value of 0.946, and most events occurring between June and July. Misclassifications mainly arise when the model detects events slightly later than their actual occurrence, possibly due to delayed NDVI decreases resulting from prior missing values.

Fig. 12 illustrates the recall for MDA II, for the different number of mowing events annotated per parcel. Among the 54 unmown parcels, approximately 79.6% were correctly identified as unmown. Furthermore, in

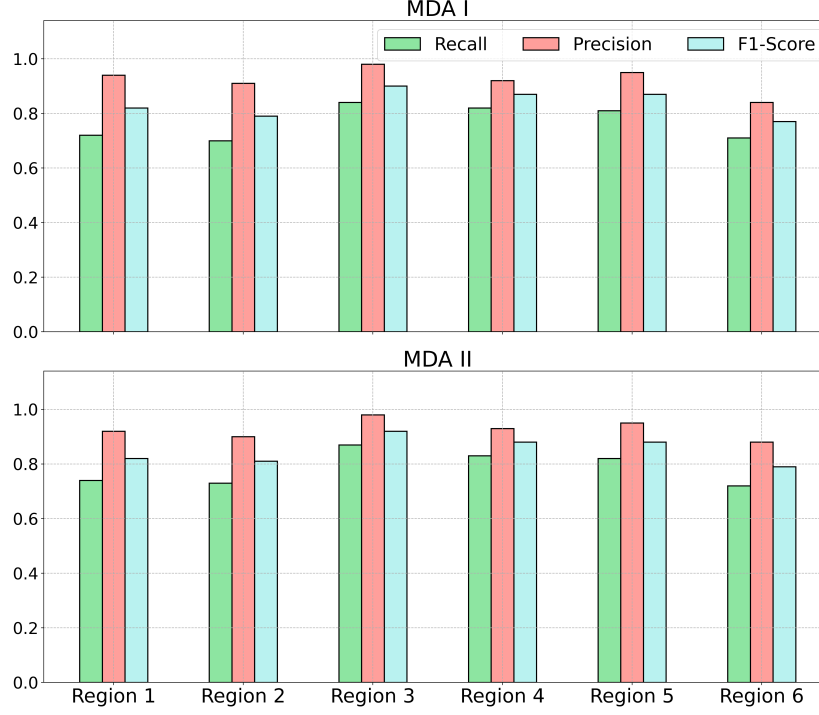


Fig. 10. Mowing detection performance (i.e., recall, precision and f1-score) over the different study regions for MDA I and MDA II, using NDVI time series produced by the proposed SF model.

parcels with a single mowing event, the recall percentage demonstrates a relatively improved performance, surpassing 85%. However, in the case of the 95 parcels with two mowing events, only in 29.5% of them the algorithm managed to accurately identified both events. Remarkably, in approximately 76% of these two-event parcels, at least one event was detected accurately.

5.3. Recovery of masked events

In Section 5.2, we assessed the impact of the SF algorithm on the two event detection methods. This section investigates cases where grassland parcel activities are unobservable through optical data (due to consecutive

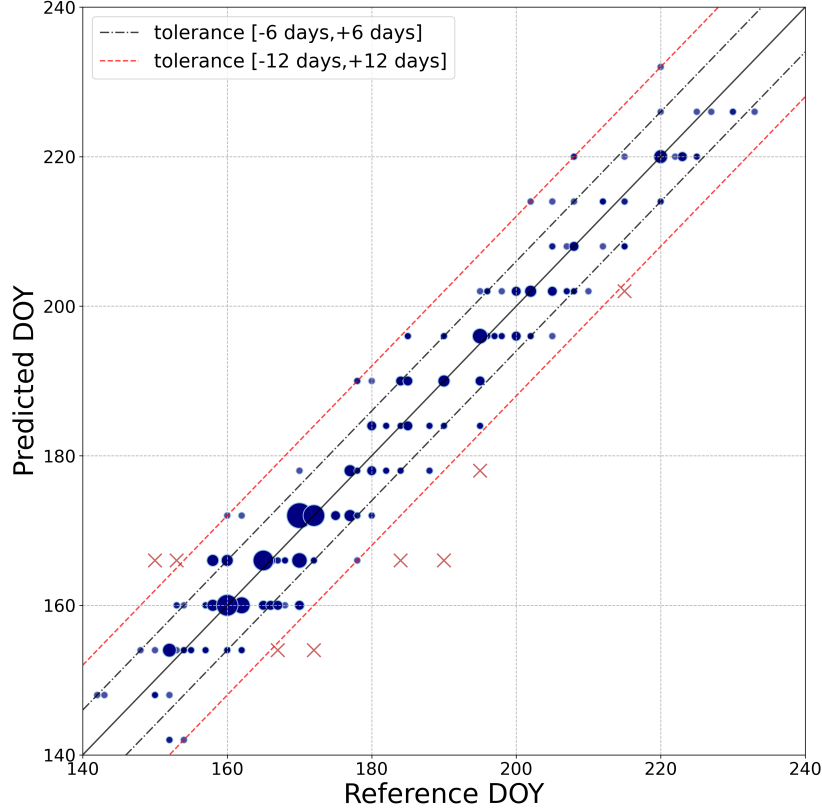


Fig. 11. Scatter plot comparing the grassland event reference Day of Year (DoY) and predicted DoY using MDA II for event prediction and SF algorithm for interpolation of the NDVI input time series. The size of each point indicates the number of observations.

cloudy observations), rendering NDVI-based detection inadequate for identifying such events. For this purpose, we selected 359 cases from the dataset with a single mowing event in order to intentionally hide them. On these cases, we artificially mask out the NDVI value from the day before the event and the following values that could reveal grassland activity (e.g., lower NDVI values). This leads to gaps of 3-7 consecutive missing values (24-48 days).

In Table 6, we compare the performance of each mowing detection al-

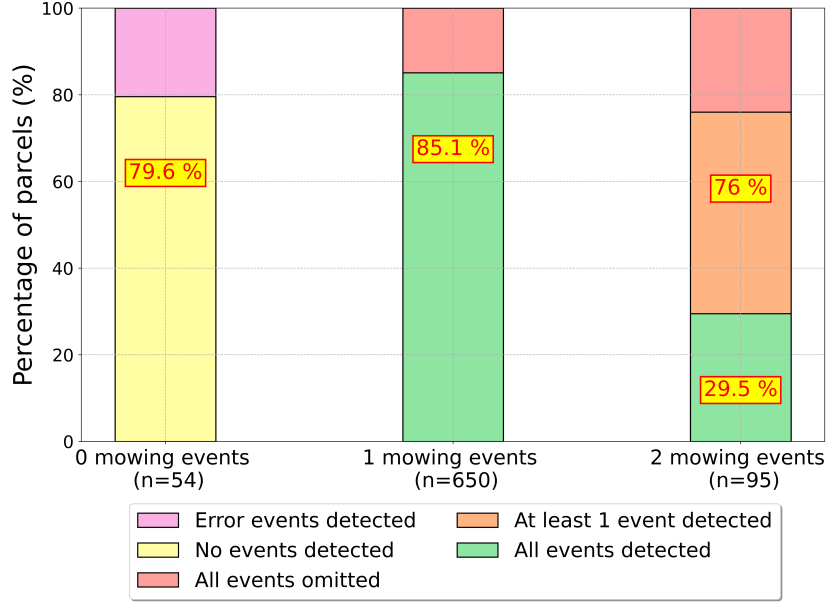


Fig. 12. Evaluation of the performance of MDA II on the different number of mowing events that occurred in parcels during the season. The first bar corresponds to the performance against non-mowed parcels, the second bar against parcels that were mowed exactly one time and the third bar for parcels that were mowed twice. For each of them the percentage of actual cases correctly identified (i.e., recall) or the portion of the actual events omission is illustrated.

gorithm applied to i) the raw NDVI series (no interpolation) and ii) the reconstructed NDVI time series using the SF model. Both algorithms perform poorly without interpolation due to lack of optical information. On the other hand, SF is able to recover nearly half of the actual events for MDA I and over half for MDA II, with relatively high precision values of 0.63 and 0.58, respectively. This demonstrates the robustness of SF in improving detection accuracy and reconstructing NDVI drops, even for large temporal gaps, making it a promising approach when optical data fails to capture event information.

Table 6

Performance of the MDA I and MDA II algorithms on detecting artificially masked out grassland mowing events, using the actual NDVI values and the reconstructing ones by utilizing the SF algorithm.

Algorithm	Interpolation	Recall	Precision	F1-score
MDA I	-	0.036	0.074	0.048
	SF	0.521	0.810	0.634
MDA II	-	0.123	0.128	0.134
	SF	0.655	0.701	0.677

In Fig. 13, we illustrate how the accuracy of event detection is affected by the time-window (tolerance) within which we consider an event as correct. The SF method reaches its optimal recall performance of around 0.5 for MDA I and 0.6 for MDA II after 8 days, which remains relatively stable for higher tolerance parameter as we are reaching the default threshold (i.e., 12 days). Interestingly, even for very low tolerance values, it achieves satisfactory performance, especially considering cases of completely hidden events. In contrast, non-interpolated NDVI time series result in extremely low recall values, irrespective of the tolerance value.

Fig. 14 provides a visual demonstration of the effectiveness of the SF algorithm in detecting mowing events in grassland areas. Specifically, it displays the actual NDVI values of a parcel during the event dates, as well as the predicted values generated by the SF algorithm. We observe a high correlation between the predictions and the actual measurements, indicating

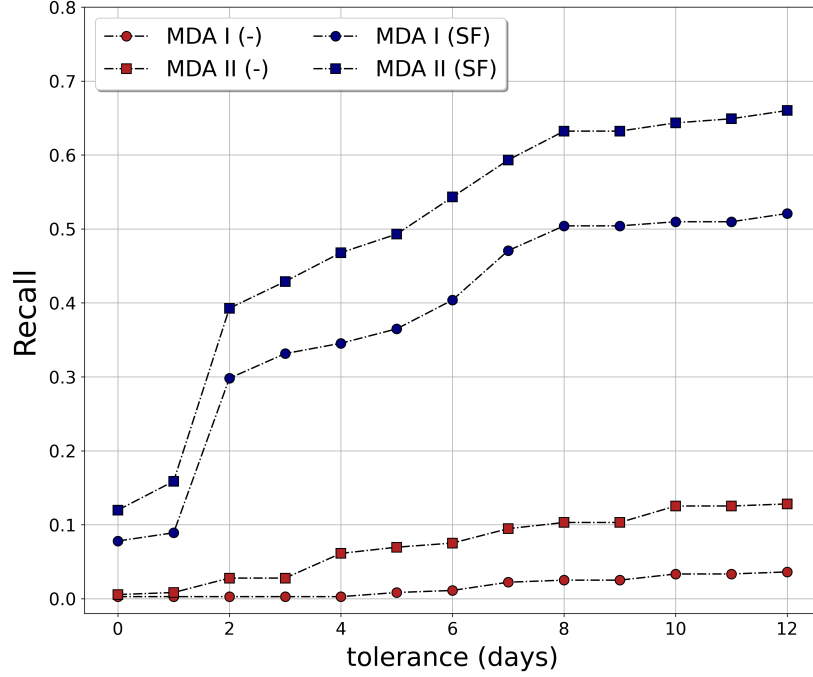


Fig. 13. Evolution of recall score using MDA I and MDA II algorithms and different time-windows (tolerance). Tolerance refers to the difference in days between the actual and the predicted event for which we consider the prediction as correct. Blue dots/squares indicate the results of MDA I/MDA II using the SF algorithm for interpolation while the red dots/squares indicate the results of MDA I/MDA II without interpolation.

the model’s effectiveness in detecting mowing events. These findings are significant for grassland sustainability as they offer detailed information about the extent and location of mowing events.

5.4. DNN mowing detection architecture

In previous sections, we have demonstrated the effectiveness of the SF algorithm in accurately reconstructing missing NDVI values in grasslands. The algorithm performed well even when missing values occurred during mowing events. We have also employed two threshold-based algorithms to

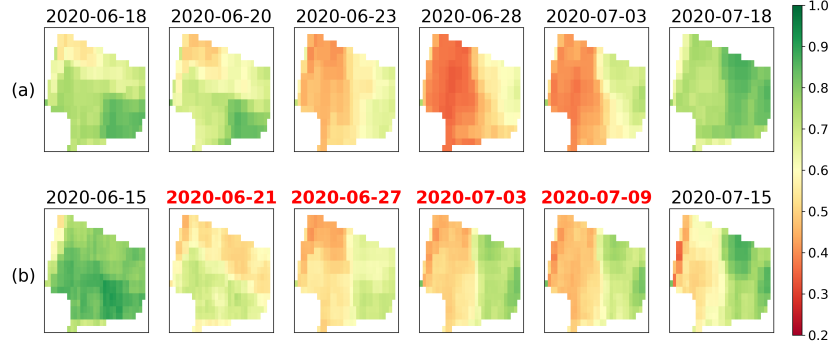


Fig. 14. Spatial visualization of NDVI time series for a parcel. (a) Actual NDVI extracted from the Sentinel-2 cloud-free acquisition dates, (b) artificial NDVI time series created after masking the values on the dates during and after the observed mowing event, which are highlighted in red (from 21/06 to 09/07)). For further visualization, refer in Fig. S8 of [Appendix A](#).

predict mowing events and evaluated the impact of using the SF algorithm on the input NDVI time series to improve prediction performance.

In this section, we utilized the SF architecture to detect mowing events (see [Section 4.4](#)) and compared its performance with the algorithms mentioned earlier. To evaluate the model, we conducted a 3-fold cross-validation using the photo-interpretation dataset (refer to [Section 3.2.2](#)). The dataset was divided into three folds at the parcel level, taking into account the date of the annotated mowing events to ensure fairness. Specifically, each fold includes parcels with a distribution of event dates that matches that of the entire dataset. However, even though we split on the parcel level, the training of the models performed at the pixel level. This approach helped us obtain reliable results for evaluating the SF architecture. Finally, for our suggested approach, which requires 6-day gap time series, we trained two models; i) in the one we used time series interpolated with AI and ii) on the other we

used the reconstructed time series using the SF model. These results were compared with the ones obtained for each MDA after applying i) the raw time series without any interpolation, ii) the same time series after Akima interpolation, and the subsequent acquisition of a 6-day temporal resolution, and iii) the corresponding results after implementing the SF model.

Table 7 displays the results on the mowing event detection task. MDA I achieved the highest recall (0.875), albeit with a relatively low precision of (0.686), resulting in suboptimal overall performance. Notably, Akima interpolation significantly improved precision without sacrificing recall. A similar trend was observed for MDA II, with a slight decrease in overall recall, leading to a substantial increase in precision. In both cases, the use of SF-derived time series resulted in significantly improved precision while maintaining similar recall levels, leading to an increased overall f1-score of approximately 0.83.

Our suggested approach outperforms threshold-based methods in identifying mowing events, especially with SF-processed NDVI input, achieving optimal results with significantly higher precision (0.83 and 0.86). In both cases of our proposed implementation, the mean f1-score exceeded 80%, indicating highly effective performance in mowing event detection. Notably, our suggested supervised approach achieved f1-score close to 85% when incorporating SF for interpolation, representing an approximately 2% increase over the Akima interpolation case. This is a significant improvement, especially given that we have used very dense NDVI time series (i.e., minimal cloud coverage), making the majority of events relatively easy to detect for both input scenarios.

Table 7

Recall, precision, and f1-score of MDA I, MDA II, and SF algorithm for the detection of grassland mowing events. The values correspond to the mean and the standard deviation scores by using a 3-fold cross-validation.

Algorithm	Interpolation	Recall	Precision	F1-score
MDA I	-	0.875 ± 0.003	0.686 ± 0.010	0.769 ± 0.007
MDA I	AI	0.841 ± 0.005	0.759 ± 0.012	0.798 ± 0.009
MDA I	SF	0.821 ± 0.005	0.834 ± 0.005	0.827 ± 0.004
MDA II	-	0.817 ± 0.006	0.763 ± 0.015	0.789 ± 0.009
MDA II	AI	0.811 ± 0.008	0.803 ± 0.014	0.807 ± 0.010
MDA II	SF	0.814 ± 0.007	0.849 ± 0.011	0.831 ± 0.006
Ours'	AI	0.829 ± 0.009	0.830 ± 0.009	0.829 ± 0.001
Ours'	SF	0.840 ± 0.004	0.855 ± 0.009	0.847 ± 0.004

6. Discussion

6.1. Cloud filtering for event detection

Cloud cover can be so extensive at times that it results in gaps in the time series that may span more than a month. In Section 5.3, we illustrated how the SF algorithm produces a continuous time series, allowing for the identification of mowing events that would have been missed if only optical imagery had been used. However, cloud masks may not always detect the presence of clouds accurately, resulting in false measurements and inaccurate event detection. According to [52], there is a trade-off between data availability and accuracy when setting the cloud cover threshold for grassland

monitoring systems, which depends on the end-user’s preferences.

Apart from reconstructing missing information, the SF methodology also serves as a supplementary cloud filtering mechanism. By incorporating SAR and optical data, we observe that it can identify and disregard available Sentinel-2 measurements that result in sudden drops of NDVI, when no correlation between the two components is justified.

In Fig 15, we illustrate a typical scenario where the sen2Cor algorithm fails to detect high cirrus clouds (mid-April), resulting in the inclusion of a noisy measurement that could potentially be misinterpreted as an event from the mowing event algorithms. As shown, the SF methodology ignores the NDVI drop, even though it was included into the algorithm’s input data and instead, it generates an output following the general upward trend.

Taking the aforementioned into account, a filtering routine can be developed. By employing a particular threshold difference between the actual NDVI value and the one generated by the SF model, timestamps that are potentially affected by clouds can be identified and excluded. This additional technique can improve the initial cloud masking process, resulting in more accurate time series data for monitoring agricultural land and making it more suitable for the subsequent tasks.

6.2. Gap-filling ablation study

To determine the individual contributions of different components within the SF model, we conducted an ablation study. This study specifically analyzed the NDVI gap-filling performance across six varied input data configurations. The baseline scenario includes all the features described earlier in Table 2, while the other five scenarios are constructed by combining specific

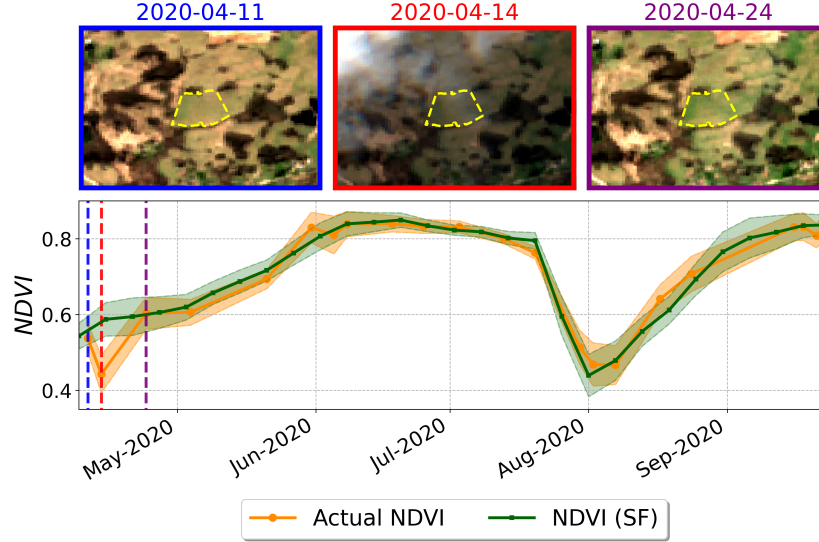


Fig. 15. Example of a case where the SF algorithm acts as a cloud filtering mechanism. The top three RGB images have been derived from consecutive Sentinel-2 captures. The first and the last are clear-sky images while the middle one suffers from high cirrus clouds. In the plot below are presented the actual NDVI time series (orange) and the predicted ones using the SF algorithm (green). The blue, red and purple vertical dotted lines refer to the dates that the aforementioned images were captured.

features, and their derived products. These scenarios involve combinations or single deployments of the σ_0 , coherence, and NDVI features to showcase various input configurations. All scenarios maintain consistent model parameter configurations and use the same training and testing pixels from the datasets (see Table 4).

Table 8 presents the MAE and R^2 of the different scenarios. The performance of the model without using as input the cloud-free NDVI time series is substantially lower. In these cases, the average MAE was more than 0.051, and the R^2 remained below 0.79. The incorporation of the available NDVI measurements leads to a significant improvement, with a decrease of

the average MAE by 26-29%, depending on the case, and an increase in R^2 by approximately 0.09, which corresponds to an increase of around 11%. Specifically, MAE gets average values below 0.04, and R^2 over 0.87. Finally, the best results were obtained with the inclusion of all derived features, as expected.

Table 8

MAE and R^2 obtained from the SF model on the masked timestamps using different combinations of the input features.

Input Features	MAE	R^2
{coherence}	0.0533 ± 0.007	0.785
$\{\sigma_0\}$	0.0529 ± 0.006	0.787
{coherence, σ_0 }	0.0518 ± 0.006	0.789
{NDVI, coherence}	0.0395 ± 0.004	0.876
{NDVI, σ_0 }	0.0389 ± 0.004	0.876
{NDVI, coherence, σ_0 }	0.0370 ± 0.004	0.881

6.3. Spatial generalization

To gain additional insights, we conducted an experiment to assess the model’s behavior when trained on a limited number of regions. This allowed us to evaluate the model’s ability to generalize spatially to regions that were not included in the original training process. Additionally, by examining how the number of training samples affects the quality of the training process, we can determine the minimum number required to achieve satisfactory results.

The optimal generalization capability of the SF model depends heavily on the size of the training dataset. To accurately learn from the distribution of missing values and fill NDVI gaps, it is crucial to have a representative sample of training instances across the entire Lithuania. Fig. 16 demonstrates the impact of increasing the number of training instances and the regions used for training on MAE. The darker colors indicate more training regions used. While including more training samples leads to a decrease in MAE, it appears that using training samples from different regions is more crucial. Interestingly, by utilizing only three regions, we can achieve near-optimal results. Despite the limited number of training regions, in many cases the model achieves near-optimal performance. This may be due to the uniform mowing policy and similar grassland management practices throughout Lithuania, resulting in similar grassland vegetation profiles. It can be also attributed to the fact that there are some regions that are larger (e.g., Region 1 and 2), which include diverse cases, and thus when they are used for training, we can more accurately represent the overall distribution. However, it’s essential to consider the cloud coverage distribution of each training region, as this can affect the model’s generalization ability beyond those regions. If the cloud coverage profile of the training samples differs significantly from the overall distribution, the model may overfit to the training regions and fail to generalize well. For more information, in the [Appendix A](#) (Table S4) we present the MAE computed on the inference subset of each region, and overall, when the model is trained on one, two, or three regions.

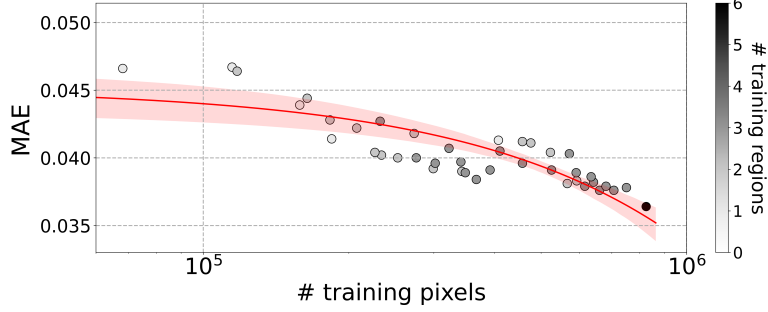


Fig. 16. Scatter plot comparing the MAE with different number of training pixels. The color of each point indicates the number of training regions, as shown in the right color bar.

6.4. Limitations and future work

In recent years, numerous studies have concentrated on employing neural networks to combine SAR and optical data to tackle the problem of discontinuous optical image time series. However, none of these studies have investigated incorporating the available optical data directly into the model’s architecture. According to [12], such an approach could potentially cause the model to ignore the remaining input features because the target and input data would be identical at several timestamps. Our observations during the training of SF using NDVI time series as an additional input feature confirmed this issue, as we noticed a high correlation between the input and output NDVI time series. To address this concern, we used temporal weighting for each input sample, as mentioned in Section 4.3.3. We assigned masked NDVI values a weight of 0.75, while non-masked values received a weight of 0.25. Moreover, we assigned a weight of 0 to any value corresponding to an interpolated timestamp, as we used interpolation to produce a complete time series.

Our selection of the CNN-RNN architecture over more advanced DNN architectures (e.g., Transformers) is motivated by the fact that it has been already suggested and applied in a similar research task [24] and it also offers a computational efficient approach. Furthermore, our primary objective was to emphasize over the contribution of integrating the Sentinel-2 measurements into the model’s feature space. Overall, we are confident that this architecture adequately presents our goal of improving the reconstruction of missing NDVI values and enhancing mowing detection accuracy. We also intend to explore a broader range of architectures in future research.

By leveraging the ability of neural networks to learn complex temporal patterns, we capture grassland phenology information and dependencies. NDVI generally requires approximately 10 days to recover half of the value lost after a grassland mowing event [8]. In Lithuania, it is uncommon to find cases where no optical cloud-free images has been captured during such long periods, especially during the summer months. The majority of these gaps occur before June, whereas most mowing events take place from early June onward. Fig. 17 depicts the temporal distribution of extended gaps. Extended gaps refer to occasions where pixels have been masked out because of cloud coverage for at least the three previous Sentinel-2 acquisitions. This duration is considered sufficient to conceal a mowing event. Consequently, while the model can effectively uncover hidden mowing events, it is important to note that, in our study, such occurrences are anticipated to be relatively infrequent (5-10%).

In Section 6.3, we showcased the generalization ability of our model across Lithuania. Our future goal is to extend this approach to other European

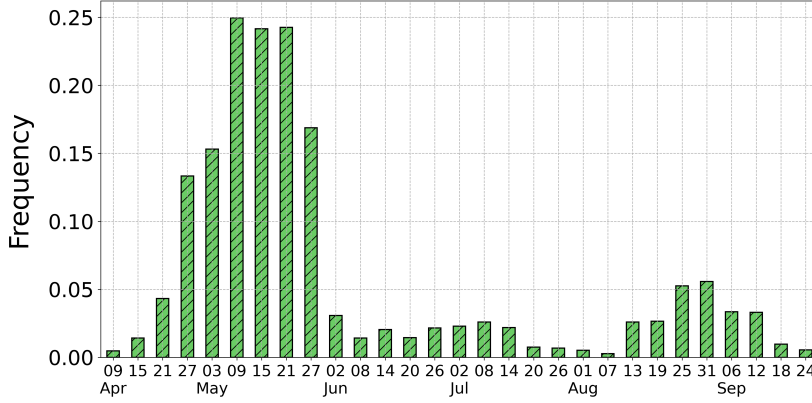


Fig. 17. Frequency of extended gaps on each date. Extended gaps are considered cases of pixels in a Sentinel-2 image that have been masked out due to cloud coverage for at least the three previous acquisitions.

countries with diverse grassland mowing and activity policies, as well as varying cloud coverage distributions. This would lead in the creation of a pan-European model that could be highly valuable for CAP monitoring.

Moreover, our approach can be adapted through minor modifications to reconstruct other remote sensing indices, such as Soil Adjusted Vegetation Index (SAVI), and Normalized Burn Ratio (NBR), or even raw optical spectral bands. These indices are particularly beneficial for monitoring vegetation or detecting farming practices, including tillage and stubble burning. Consequently, a more versatile methodology can be developed to generate one or multiple relevant indices, depending on the task. Furthermore, monitoring various land cover vegetation types is possible, including forests, arable croplands (such as wheat, maize, or barley) and orchards.

Finally, the implementation of the SF algorithm (see Section 4.4) for the detection of mowing events appears very promising, and we plan to con-

duct further evaluation of its potential in the future. Specifically, it will be additionally incorporated and tested within the “mowing detection inter-comparison exercise” (MODCiX). This initiative aims to evaluate various mowing detection algorithms using openly accessible satellite data across Europe under a common validation system.

7. Conclusion

The Sentinel-2 satellite missions provide frequent optical images for the continuous monitoring of grassland activity. However, relying on optical images alone for monitoring is restricted by cloud coverage. To overcome this limitation, we proposed a CNN-RNN deep learning architecture that makes use of all available cloud-free optical images (Sentinel-2), along with weather-independent SAR data (Sentinel-1), to create continuous NDVI time series for grassland fields, with a temporal resolution of 6 days. The model has been trained on six different regions of Lithuania to account for different cloud coverage profiles and agro-climatic conditions.

The results showed that our method performed better than alternative gap-filling techniques (linear, Akima, quadratic interpolation) when evaluated across various scenarios to demonstrate its transferability and generalization capacity. Additionally, we assessed the importance of the generated continuous NDVI time series for the downstream task of grassland mowing event detection. The outcomes suggest that our methodology significantly improves the detection accuracy by i) identifying events that would have otherwise gone undetected and ii) eliminating instances of false event predictions caused by cloud presence.

Finally, we investigated our model’s capacity to detect grassland mowing events. Overall, the outcomes are promising, with f1-score of 85%, surpassing the performance of the two baseline methodologies by more than 6%.

CRedit authorship contribution statement

Iason Tsardanidis: Conceptualization, Methodology, Software, Validation, Formal Analysis, Investigation, Data Curation, Visualization, Writing – original draft, Writing – review & editing. **Alkiviadis Koukos:** Conceptualization, Methodology, Validation, Formal Analysis, Data Curation, Visualization, Writing – review & editing. **Vasileios Sitokonstantinou:** Supervision, Conceptualization, Formal Analysis, Writing – review & editing. **Thanassis Drivas:** Software, Data Curation, Writing – review & editing. **Charalampos Kontoes:** Supervision, Writing – review & editing, Funding acquisition.

Declaration of Competing Interest

The authors declare that they have no known competing financial interests or personal relationships that could have appeared to influence the work reported in this paper.

Acknowledgements

This work has been supported by the ENVISION and CALLISTO projects, funded by European Union’s Horizon 2020 research and innovation programmes under grant agreements No. 869366 and No. 101004152.

Data availability

Data will be made available on request.

Appendix A. Supplementary Material

Supplementary material is available at [zenodo](#).

References

- [1] F. P. O'Mara, The role of grasslands in food security and climate change, *Annals of Botany* 110 (6) (2012) 1263–1270. [doi:https://doi.org/10.1093/aob/mcs209](https://doi.org/10.1093/aob/mcs209).
- [2] Y. Zhao, Z. Liu, J. Wu, Grassland ecosystem services: a systematic review of research advances and future directions, *Landscape Ecology* 35 (2020) 793–814. [doi:https://doi.org/10.1007/s10980-020-00980-3](https://doi.org/10.1007/s10980-020-00980-3).
- [3] R. D'Andrimont, G. Lemoine, M. Van der Velde, Targeted grassland monitoring at parcel level using sentinels, street-level images and field observations, *Remote Sensing* 10 (2018) 1300. [doi:https://doi.org/10.3390/rs10081300](https://doi.org/10.3390/rs10081300).
- [4] S. Reinermann, S. Asam, U. Gessner, T. Ullmann, C. Kuenzer, Multi-annual grassland mowing dynamics in germany: spatio-temporal patterns and the influence of climate, topographic and socio-political conditions, *Frontiers in Environmental Science* 11 (2023). [doi:https://doi.org/10.3389/fenvs.2023.1040551](https://doi.org/10.3389/fenvs.2023.1040551).

- [5] I. Ali, F. Cawkwell, E. Dwyer, B. Barrett, S. Green, Satellite remote sensing of grasslands: from observation to management, *Journal of Plant Ecology* 9 (6) (2016) 649–671. doi:<https://doi.org/10.1093/jpe/rtw005>.
- [6] M. Gómez Giménez, R. de Jong, R. Della Peruta, A. Keller, M. E. Schaepman, Determination of grassland use intensity based on multi-temporal remote sensing data and ecological indicators, *Remote Sensing of Environment* 198 (2017) 126–139. doi:<https://doi.org/10.1016/j.rse.2017.06.003>.
- [7] S. Estel, S. Mader, C. Levers, P. Verburg, M. Baumann, T. Kuemmerle, Combining satellite data and agricultural statistics to map grassland management intensity in europe, *Environmental Research Letters* 13 (7) (2018) 074020. doi:<https://doi.org/10.1088/1748-9326/aacc7a>.
- [8] N. Kolečka, C. Ginzler, R. Pazur, B. Price, P. H. Verburg, Regional scale mapping of grassland mowing frequency with sentinel-2 time series, *Remote Sensing* 10 (2018) 1221. doi:<https://doi.org/10.3390/rs10081221>.
- [9] P. Griffiths, C. Nendel, J. Pickert, P. Hostert, Towards national-scale characterization of grassland use intensity from integrated sentinel-2 and landsat time series, *Remote Sensing of Environment* 238 (2020) 111124. doi:<https://doi.org/10.1016/j.rse.2019.03.017>.
- [10] M. Sudmanns, D. Tiede, H. Augustin, S. Lang, Assessing global sentinel-2 coverage dynamics and data availability for operational earth obser-

- vation (eo) applications using the eo-compass, *International Journal of Digital Earth* 13 (7) (2020) 768–784. doi:<https://doi.org/10.1080/17538947.2019.1572799>.
- [11] J. Li, C. Li, W. Xu, H. Feng, F. Zhao, H. Long, Y. Meng, W. Chen, H. Yang, G. Yang, Fusion of optical and sar images based on deep learning to reconstruct vegetation ndvi time series in cloud-prone regions, *International Journal of Applied Earth Observation and Geoinformation* 112 (2022) 102818. doi:<https://doi.org/10.1016/j.jag.2022.102818>.
- [12] A. Garioud, S. Valero, S. Giordano, C. Mallet, Recurrent-based regression of sentinel time series for continuous vegetation monitoring, *Remote Sensing of Environment* 263 (2021) 112419. doi:<https://doi.org/10.1016/j.rse.2021.112419>.
- [13] C. Zeng, H. Shen, L. Zhang, Recovering missing pixels for landsat etm+ slc-off imagery using multi-temporal regression analysis and a regularization method, *Remote Sensing of Environment* 131 (2013) 182–194. doi:<https://doi.org/10.1016/j.rse.2012.12.012>.
- [14] M. Fauvel, M. Lopes, T. Dubo, J. Rivers-Moore, P.-L. Frison, N. Gross, A. Ouin, Prediction of plant diversity in grasslands using sentinel-1 and -2 satellite image time series, *Remote Sensing of Environment* 237 (2020) 111536. doi:<https://doi.org/10.1016/j.rse.2019.111536>.
- [15] V. Sitokonstantinou, A. Koukos, T. Drivas, C. Kontoes, I. Papoutsis, V. Karathanassi, A scalable machine learning pipeline for paddy rice

- classification using multi-temporal sentinel data, *Remote Sensing* 13 (9) (2021) 1769. doi:<https://doi.org/10.3390/rs13091769>.
- [16] Álvaro Moreno-Martínez, E. Izquierdo-Verdiguier, M. P. Maneta, G. Camps-Valls, N. Robinson, J. Muñoz-Marí, F. Sedano, N. Clinton, S. W. Running, Multispectral high resolution sensor fusion for smoothing and gap-filling in the cloud, *Remote Sensing of Environment* 247 (2020) 111901. doi:<https://doi.org/10.1016/j.rse.2020.111901>.
- [17] X. Zhu, E. H. Helmer, F. Gao, D. Liu, J. Chen, M. A. Lefsky, A flexible spatiotemporal method for fusing satellite images with different resolutions, *Remote Sensing of Environment* 172 (2016) 165–177. doi:<https://doi.org/10.1016/j.rse.2015.11.016>.
- [18] Y. Sadeh, X. Zhu, D. Dunkerley, J. P. Walker, Y. Zhang, O. Rozenstein, V. Manivasagam, K. Chenu, Fusion of sentinel-2 and planetscope time-series data into daily 3 m surface reflectance and wheat lai monitoring, *International Journal of Applied Earth Observation and Geoinformation* 96 (2021) 102260. doi:<https://doi.org/10.1016/j.jag.2020.102260>.
- [19] M. Claverie, J. Ju, J. G. Masek, J. L. Dungan, E. F. Vermote, J.-C. Roger, S. V. Skakun, C. Justice, The harmonized landsat and sentinel-2 surface reflectance data set, *Remote Sensing of Environment* 219 (2018) 145–161. doi:<https://doi.org/10.1016/j.rse.2018.09.002>.
- [20] C.-a. Liu, Z.-X. Chen, S. Yun, J.-s. Chen, T. Hasi, H.-z. PAN, Research advances of sar remote sensing for agriculture applications: A review,

- Journal of Integrative Agriculture 18 (3) (2019) 506–525. doi:[https://doi.org/10.1016/S2095-3119\(18\)62016-7](https://doi.org/10.1016/S2095-3119(18)62016-7).
- [21] D. Mandal, V. Kumar, D. Ratha, S. Dey, A. Bhattacharya, J. M. Lopez-Sanchez, H. McNairn, Y. S. Rao, Dual polarimetric radar vegetation index for crop growth monitoring using sentinel-1 sar data, Remote Sensing of Environment 247 (2020) 111954. doi:<https://doi.org/10.1016/j.rse.2020.111954>.
 - [22] M. Ioannidou, A. Koukos, V. Sitokonstantinou, I. Papoutsis, C. Kontoes, Assessing the added value of sentinel-1 polsar data for crop classification, Remote Sensing 14 (22) (2022) 5739. doi:<https://doi.org/10.3390/rs14225739>.
 - [23] K. Voormansik, T. Jagdhuber, K. Zalite, M. Noorma, I. Hajnsek, Observations of cutting practices in agricultural grasslands using polarimetric sar, IEEE Journal of Selected Topics in Applied Earth Observations and Remote Sensing 9 (4) (2016) 1382–1396. doi:<https://doi.org/10.1109/JSTARS.2015.2503773>.
 - [24] W. Zhao, Y. Qu, J. Chen, Z. Yuan, Deeply synergistic optical and sar time series for crop dynamic monitoring, Remote Sensing of Environment 247 (2020) 111952. doi:<https://doi.org/10.1016/j.rse.2020.111952>.
 - [25] H. Shen, X. Li, Q. Cheng, C. Zeng, G. Yang, H. Li, L. Zhang, Missing information reconstruction of remote sensing data: A technical review,

- IEEE Geoscience and Remote Sensing Magazine 3 (3) (2015) 61–85.
doi:<https://doi.org/10.1109/MGRS.2015.2441912>.
- [26] S. Li, L. Xu, Y. Jing, H. Yin, X. Li, X. Guan, High-quality vegetation index product generation: A review of ndvi time series reconstruction techniques, *International Journal of Applied Earth Observation and Geoinformation* 105 (2021) 102640. doi:<https://doi.org/10.1016/j.jag.2021.102640>.
- [27] Y. Julien, J. A. Sobrino, Optimizing and comparing gap-filling techniques using simulated ndvi time series from remotely sensed global data, *International Journal of Applied Earth Observation and Geoinformation* 76 (2019) 93–111. doi:<https://doi.org/10.1016/j.jag.2018.11.008>.
- [28] J. Wang, X. Xiao, R. Bajgain, P. Starks, J. Steiner, R. B. Doughty, Q. Chang, Estimating leaf area index and above ground biomass of grazing pastures using sentinel-1, sentinel-2 and landsat images, *ISPRS Journal of Photogrammetry and Remote Sensing* 154 (2019) 189–201. doi:<https://doi.org/10.1016/j.isprsjprs.2019.06.007>.
- [29] L. Pipia, J. Muñoz-Marí, E. Amin, S. Belda, G. Camps-Valls, J. Verrelst, Fusing optical and sar time series for lai gap filling with multioutput gaussian processes, *Remote Sensing of Environment* 235 (2019) 111452. doi:<https://doi.org/10.1016/j.rse.2019.111452>.
- [30] E. P. Dos Santos, D. D. da Silva, C. H. do Amaral, E. I. Fernandes-Filho, R. L. S. Dias, A machine learning approach to reconstruct cloudy

- affected vegetation indices imagery via data fusion from sentinel-1 and landsat 8, *Computers and Electronics in Agriculture* 194 (2022) 106753. doi:<https://doi.org/10.1016/j.compag.2022.106753>.
- [31] M. Fuentes Reyes, S. Auer, N. Merkle, C. Henry, M. Schmitt, Sar-to-optical image translation based on conditional generative adversarial networks—optimization, opportunities and limits, *Remote Sensing* 11 (17) (2019) 2067. doi:<https://doi.org/10.3390/rs11172067>.
- [32] A. Meraner, P. Ebel, X. X. Zhu, M. Schmitt, Cloud removal in sentinel-2 imagery using a deep residual neural network and sar-optical data fusion, *ISPRS Journal of Photogrammetry and Remote Sensing* 166 (2020) 333–346. doi:<https://doi.org/10.1016/j.isprsjprs.2020.05.013>.
- [33] M. Rußwurm, M. Körner, Multi-temporal land cover classification with sequential recurrent encoders, *ISPRS International Journal of Geo-Information* 7 (4) (2018) 129. doi:<https://doi.org/10.3390/ijgi7040129>.
- [34] D. Ienco, R. Interdonato, R. Gaetano, D. H. T. Minh, Combining sentinel-1 and sentinel-2 satellite image time series for land cover mapping via a multi-source deep learning architecture, *ISPRS Journal of Photogrammetry and Remote Sensing* 158 (2019) 11–22. doi:<https://doi.org/10.1016/j.isprsjprs.2019.09.016>.
- [35] M. O. Turkoglu, S. D’Aronco, G. Perich, F. Liebisch, C. Streit, K. Schindler, J. D. Wegner, Crop mapping from image time series: Deep learning with multi-scale label hierarchies, *Remote Sensing of En-*

- vironment 264 (2021) 112603. doi:<https://doi.org/10.1016/j.rse.2021.112603>.
- [36] I. Ali, B. Barrett, F. Cawkwell, S. Green, E. Dwyer, M. Neumann, Application of repeat-pass terrasar-x staring spotlight interferometric coherence to monitor pasture biophysical parameters: Limitations and sensitivity analysis, *IEEE Journal of Selected Topics in Applied Earth Observations and Remote Sensing* 10 (7) (2017) 3225–3231. doi:<https://doi.org/10.1109/JSTARS.2017.2679761>.
- [37] T. Tamm, K. Zalite, K. Voormansik, L. Talgre, Relating sentinel-1 interferometric coherence to mowing events on grasslands, *Remote Sensing* 8 (2016) 802. doi:<https://doi.org/10.3390/rs8100802>.
- [38] S. Reinermann, U. Gessner, S. Asam, T. Ullmann, A. Schucknecht, C. Kuenzer, Detection of grassland mowing events for germany by combining sentinel-1 and sentinel-2 time series, *Remote Sensing* 14 (7) (2022) 1647. doi:<https://doi.org/10.3390/rs14071647>.
- [39] M. De Vroey, L. de Vendictis, M. Zavagli, S. Bontemps, D. Heymans, J. Radoux, B. Koetz, P. Defourny, Mowing detection using sentinel-1 and sentinel-2 time series for large scale grassland monitoring, *Remote Sensing of Environment* 280 (2022) 113145. doi:<https://doi.org/10.1016/j.rse.2022.113145>.
- [40] F. Lobert, A.-K. Holtgrave, M. Schwieder, M. Pause, J. Vogt, A. Gocht, S. Erasmi, Mowing event detection in permanent grasslands: Systematic evaluation of input features from sentinel-1, sentinel-2, and landsat 8

- time series, *Remote Sensing of Environment* 267 (2021) 112751. doi:
<https://doi.org/10.1016/j.rse.2021.112751>.
- [41] M. Lange, H. Feilhauer, I. Kühn, D. Doktor, Mapping land-use intensity of grasslands in germany with machine learning and sentinel-2 time series, *Remote Sensing of Environment* 277 (2022) 112888. doi:<https://doi.org/10.1016/j.rse.2022.112888>.
- [42] A.-K. Holtgrave, F. Lobert, S. Erasmi, N. Röder, B. Kleinschmit, Grassland mowing event detection using combined optical, sar, and weather time series, *Remote Sensing of Environment* 295 (2023) 113680. doi:<https://doi.org/10.1016/j.rse.2023.113680>.
- [43] A. Laurinavičius, D. Čygas, A. Vaitkus, T. Ratkevičius, Climatic regioning of lithuania from the point of view of winter road maintenance, in: XIV th International Winter Road Congress, 2014, pp. 1–9.
- [44] M. Pinheiro, N. Miranda, A. Recchia, A. Cotrufo, N. Franceschi, R. Piantanida, K. Schmidt, C. Gisinger, G. Hajduch, P. Vincent, Sentinel-1 instruments status and product performance update for 2022, in: EU-SAR 2022; 14th European Conference on Synthetic Aperture Radar, VDE, 2022, pp. 1–5.
- [45] J. Louis, B. Pflug, M. Main-Knorn, V. Debaecker, U. Mueller-Wilm, R. Q. Iannone, E. Giuseppe Cadau, V. Boccia, F. Gascon, Sentinel-2 global surface reflectance level-2a product generated with sen2cor, in: IGARSS 2019 - 2019 IEEE International Geoscience and Remote Sens-

- ing Symposium, 2019, pp. 8522–8525. doi:<https://10.1109/IGARSS.2019.8898540>.
- [46] T. Drivas, V. Sitokonstantinou, I. Tsardanidis, A. Koukos, C. Kontoes, V. Karathanassi, A data cube of big satellite image time-series for agriculture monitoring, in: 2022 IEEE 14th Image, Video, and Multidimensional Signal Processing Workshop (IVMSP), 2022, pp. 1–5. doi:<https://doi.org/10.1109/IVMSP54334.2022.9816291>.
- [47] K. Tarrio, X. Tang, J. G. Masek, M. Claverie, J. Ju, S. Qiu, Z. Zhu, C. E. Woodcock, Comparison of cloud detection algorithms for sentinel-2 imagery, *Science of Remote Sensing* 2 (2020) 100010. doi:<https://doi.org/10.1016/j.srs.2020.100010>.
- [48] V. Komisarenko, K. Voormansik, R. El Shawi, S. Sakr, Exploiting time series of sentinel-1 and sentinel-2 to detect grassland mowing events using deep learning with reject region, *Scientific Reports* 12 (2022) 983. doi:<https://doi.org/10.1038/s41598-022-04932-6>.
- [49] C. Watzig, A. Schaumberger, A. Klingler, A. Dujakovic, C. Atzberger, F. Vuolo, Grassland cut detection based on sentinel-2 time series to respond to the environmental and technical challenges of the austrian fodder production for livestock feeding, *Remote Sensing of Environment* 292 (2023) 113577. doi:<https://doi.org/10.1016/j.rse.2023.113577>.
- [50] H. Akima, A new method of interpolation and smooth curve fitting based on local procedures, *Journal of the ACM (JACM)* 17 (4) (1970) 589–602. doi:<https://doi.org/10.1145/321607.321609>.

- [51] M. Schwieder, M. Wesemeyer, D. Frantz, K. Pfoch, S. Erasmi, J. Pickert, C. Nendel, P. Hostert, Mapping grassland mowing events across germany based on combined sentinel-2 and landsat 8 time series, *Remote Sensing of Environment* 269 (2022) 112795. doi:<https://doi.org/10.1016/j.rse.2021.112795>.
- [52] T. Hardy, L. Kooistra, M. Domingues Franceschini, S. Richter, E. Vonk, G. van den Eertwegh, D. Van Deijl, Sen2grass: A cloud-based solution to generate field-specific grassland information derived from sentinel-2 imagery, *AgriEngineering* 3 (1) (2021) 118–137. doi:<https://doi.org/10.3390/agriengineering3010008>.